Chapter

ZINC-RICH PAINT COATINGS CONTAINING EITHER IONIC SURFACTANT-MODIFIED OR FUNCTIONALIZED MULTI-WALLED CARBON NANOTUBE-SUPPORTED POLYPYRROLE UTILIZED TO PROTECT COLD-ROLLED STEEL AGAINST CORROSION

András Gergely[1,], Tamás Török[2], Zoltán Pászti[3], Imre Bertóti[4], Judith Mihály[5] and Erika Kálmán[1]*

[1]Department of Surface Modification and Nanostructures, Institute of Nanochemistry and Catalysis, Chemical Research Center of the Hungarian Academy of Sciences, Budapest, Hungary
[2]Department of Metallurgical and Foundry Engineering, Faculty of Materials Science and Engineering, University of Miskolc, Hungary
[3]Laboratory of Hydrogen Energy, Institute of Nanochemistry and Catalysis, Chemical Research Center of the Hungarian Academy of Sciences, Budapest, Hungary
[4]Department of Plasma Chemistry, Institute of Materials and Environmental Chemistry, Chemical Research Center of the Hungarian Academy of Sciences, Budapest, Hungary
[5]Department of Biological Nanochemistry, Institute of Nanochemistry and Catalysis, Chemical Research Center of the Hungarian Academy of Sciences, Budapest, Hungary

ABSTRACT

The intense anodic action of sacrificial zinc pigments ensured viable galvanic function of the highly porous liquid zinc-rich paints (ZRPs) result in deteriorated long-term corrosion resistance often accompanied by cathodic delamination phenomena. In our approach, such a efficacy problem related to the corrosion preventive function of ZRPs is addressed by the application of intimately structured anodic inhibitor particles composed of nano-size alumina and either polyelectrolyte-modified or chemically functionalized multi-walled carbon nanotubes (MWCNT) supported polypyrrole (PPy) in one specific zinc-rich hybrid paint formulation providing balanced active–passive protective functionality.

High dispersity of the nanotube-free PPy-deposited inhibitor particles (PDIPs) with uneven polymer distribution on the alumina carrier was confirmed by transmission

* * E-mail: doohan11@chemres.hu.

electron microscopy (TEM) observations. Furthermore, the MWCNT-embedded PDIPs indicated almost complete surface coverage of the alumina-nanotube carriers by PPy with decreased microstructure dispersity which is attributed to the effect of double-flocculants type co-deposition of the oppositely charged polymers causing coalescence of the modified particles. Depending on the amount of the nanotubes and their proportion to the quantities of the deposited PPy and polyelectrolyte as well as the concentration of the surfactant, varied micron-scale association of the PDIPs in the suspensions of dissolved alkyd matrix was disclosed by rheology characterization carried out at particular solid contents similar to hybrid paint formulation. The evenly distributed but less densely packed nano-structure of PPy was evidenced on the polyelectrolyte-modified nanotubes by Fourier-transform infrared (FTIR) spectroscopy whereas more compact polymer film formation was confirmed on the surface of functionalized nanotubes. According to the greater electrical conductivity, enhanced electroactivity and reversibility of the nanotube-embedded PDIPs were indicated over the nanotube-free particles by cyclic voltammetry, depending on the type and the amount of the nanotubes and their modification.

Protection function of the hybrid paint coatings (formulated with spherical zinc pigment at 70 wt.%) was investigated by immersion and salt-spray chamber tests over 254 and 142 day periods, respectively. Firm barrier nature of the nanotube-embedded PDIP contained hybrids was proved by electrochemical impedance spectroscopy (EIS) and radio-frequency glow-discharge optical-emission-spectroscopy (RF-GD-OES). Furthermore, due to the increased conductivity of the nanotube-embedded PDIPs cemented in epoxy primers optimally at 0.4 and 0.6 wt.%, altered corrosion preventive behaviour of the hybrid coatings was indicated by the positively polarized open-circuit potentials (OCPs) and the X-ray photoelectron spectroscopy (XPS) detected lower relative quantities of the interfacially accumulated zinc corrosion products, moderate oxidative degradation of the epoxy vehicle. Decreasing oxidative conversion of iron at the surface was indicated by XPS found to correlate with the increasing intensity of zinc corrosion and decreasing oxidative degradation of the epoxy binder, according to the higher nanotube contents of hybrid coatings. In addition, inhibited zinc corrosion caused low rate of oxidative degradation of epoxy, allowing increased durability of coating adhesion and cohesion thereby ensuring reliable protection by zinc-rich compositions.

As a conclusion, modified or functionalized MWCNTs acting as unexchangeable doping agents promote enhanced reversibility and increased conductivity of PPy, forming nano-size inhibitor particles with advanced features. Thus, such inhibitor nano-particles in zinc-rich hybrid compositions afford improved barrier and high efficiency galvanic–cathodic corrosion preventive function, exceeding long-term protection capability of the conventional ZRPs.

INTRODUCTION

The number of applications related to ZRPs is due to the exceptional protection behaviour and preventive performance afforded to steel alloys against corrosion. Traditional liquid ZRPs comprise around 90 wt.% of spherical anodic zinc pigments to ensure viable cathodic protection of metallic substrates. The diminishing galvanic function over long test periods is associated with the decreased surface area ratio of zinc and the substrate as a consequence of the intense zinc corrosion and the loss of electric contacts between anodic pigments [1]. However, passive protection function is sustained based on the enhanced barrier nature of the coating reinforced by the accumulated zinc corrosion products. This is due to the fact that zinc oxide passivates the surface of zinc pigments and inhibits the chloride-induced corrosion by sealing coating pores [2]. Thus, several zinc-rich compositions were investigated

in detail examining the effect of the binder [3], focusing on the size and shape of the anodic pigments [4-7], as well as paint formulations with various pigment compositions [8]. Lots of work has been devoted to improve protection function of the ZRPs by delaying the fading strong cathodic polarization – galvanic immunization of metallic substrates [9,10], achieving progress by alternative formulations [11,12] using organic [13,14] or inorganic binders [15,16]. Amid strict environmental regulations, any development in the field of metal-rich coatings is urged to take place to lessen the amount of zinc in primers, owing to toxicity reasons [17]. On the other hand, this is required to undergo to meet industry demand for wide selection of reliable choices whilst targeting growing consumer interests for high performance solutions.

Despite the reliable corrosion resistive behaviour, there are number of factors limiting the protection durability of ZRPs [8,11] such as electrical conductivity of the primers. Furthermore, ionic conductivity of the coatings alters the accessibility of anodic pigments since their corrosion is varied, whereas additives can mitigate the effects of organic vehicle degradation processes. Having a strong influence on active–passive function of the ZRPs [9], percolation and porosity of the primers are connected to the pigment volume concentration (PVC) and its ratio to the critical CPVC which depends on the morphology of anodic pigments having enormous effect on the protection performance [15]. Although, lamellar pigments are better than spherical ones but their combination lead to coatings performing even better because of the resultant feature of low electrical percolation threshold and the increased surface energy based intense anodic action of pigments and the related enhanced galvanic function of the coatings [12]. Primers containing zinc above 80 wt.% provides fine active protection but contents between 60 and 70 wt.% showed no valuable barrier nature or galvanic action [11]. Furthermore, the efficacy of long-term galvanic function may utterly be impaired because of the early deadhesion phenomenon (cohesive failure of binder at the interface [18]) recognized as cathodic delamination. The corrosion-induced cathodic deadhesion of ZRPs is a result of interfacial electron transfer reactions, evolution of oxidative intermediates and the formation of nucleophile agents (in the course of cathodic reactions) along with the accumulation of corrosion products. Reactive agents provoke oxidative degradation of the organic vehicles in the forms of growing yield of oxidized spices, mainly carboxyl moieties. Nonetheless, cathodic delamination can be controlled by additives mitigating the effect of alkaline pH on the organic binders [19].

Aside from addressing the porosity related issues of the ZRPs by introducing intrinsically conducting polymers (ICPs) as auxiliary inhibitors helping to substitute a part of the high zinc content [20], further improvements have been made using free-standing ICPs [21] in zinc-rich compositions obtaining organic–inorganic hybrid coatings with improved protection functionalities [20,22]. Enhanced barrier nature of the hybrids and the inhibited sacrificial and self-corrosion of anodic pigments [23,24] are attributed to the effect of anodic ICPs applied either as carrier supported additives in inorganic matrix [25] or stand-alone alternative in zinc-rich powder coatings [26]. The notion to combine ICPs with anodic pigments in hybrids arises from retaining galvanic and enhancing barrier nature of the ZRPs [22]. As a consequence, PPy is a worthy candidate to be utilized in hybrid coatings due to their ability to inhibit zinc corrosion [27] and enhance coating barrier functionality especially in the form of highly dispersed, nano-sized particles [26,28]. Inhibition function of PPy usually requires its partially oxidized form doped with unexchangeable counter ions [29,30]. On the other hand,

undoped ICPs are more beneficial to be used in coatings [31,32] due to the advantage of optimal compatibility with the organic vehicles. However, long-term protection by PPy faces tough challenges in terms of rapidly fading conductivity and redox-activity. In addition, one of the toughest challenges related to coating preparations is the dispersity of ICPs in various matrices [33] which can be resolved by using carrier-supported polymers [34-36] to obtain highly dispersed particles with increased electroactivity, conductivity and processibility [37] with improved corrosion protection abilities [38].

In these aspects, nano-size alumina and MWCNT-supported PPy is applied in epoxy paint coatings to obviate any wetting or dispersability issues. Polyelectrolyte modification and functionalisation of the nanotubes serve as an unexchangeable polymer doping which in turn promotes matrix compatibilization, high dispersity and even distribution of the inhibitor particles.

In this chapter, the application of nano-size anodic inhibitor particles is investigated in zinc-rich paint compositions analyzing the contribution of the various particles to the protection mechanism of zinc-rich primers. Thus, experimental results are presented focusing on the micro and nanostructure, spectroscopic characteristics and electroactivity of the polypyrrole-modified inhibitor particles. Corrosion resistive function of the hybrid coatings is discussed to gain adequate interpretation about the synergistic effects of the MWCNT-embedded PDIPs contained paint compositions.

EXPERIMENTAL

Preparation of Polypyrrole-Deposited Alumina/MWCNT Inhibitor Particles

The 1-amino-2-naphthol-4-sulfonic acid was used as precursor to functionalise NC7000 nanotube (Nanocyl s.a., Belgium) with naphthol-sulfonic acid through diazotation activation and coupling procedure. Decomposition of the diazonium salt was initiated by quantitative amount of ammonium iron(II) sulphate. The reaction was carried out in aqueous acetic acid at 0 °C for 12 h. Then the solid was filtrated, washed thoroughly with essential acetic acid and dried. Chemically grafted nanotubes were dispersed in oleum (20 wt.%) by 10 min ultrasonication. Then the mixture was vigorously stirred and refluxed for either 2 or 5 h at 130 °C to alter the extent of nanotube functionalisation. Finally, the suspension was poured onto ice, neutralized with sodium carbonate solution and the solid was dialyzed for three times. Thus, low and highly sulfonated nanotube samples were obtained which are referred to as LS and HS NC7000, respectively. These samples contained sulphur atom at 0.4 and 1 atomic % detected by XPS in the form of carbon bound sulfonate and sulphate groups.

Modification of the NC7000 and MWNT-30 (Shenzhen Nanotech Port Co. Ltd., China) nanotubes was performed by 30 min ultrasonication in aqueous ethanol and acetic acid dispersion (volume mixture of 10:1:3) containing polyelectrolyte like poly(4-ammonium styrene-sulfonic acid, Aldrich) and ionic surfactants such as sodium dodecyl sulphate (Aldrich) referred to as PSS and SDS, respectively. For the preparation of inhibitor particles, pyrrole (Aldrich) was dissolved in the water dispersed sol of fumed alumina (AluC, Evonik Industries AG, Germany) and the colloid was stirred intensively for 2 h. In the case of sample *p2*, the procedure of polymerisation and deposition was carried out in aqueous ethanol (at a content of 13% by volume) dispersed alumina sol. As an oxidative agent of pyrrole monomer,

the solution of iron(III) nitrate (Fluka) was added to the vigorously stirred sol in one step. When the mixture became homogeneous, 1M nitric acid solution (~1 ml) was added immediately to set the pH to 3 (for the sake of optimally balanced conditions to realize highly dispersed and stable alumina sol, moderate rate of pyrrole polymerisation with compact PPy structure and high deposition yield). Then the mixture was stirred slowly for 6 h then let stagnant for 16 h. Suspensions were filtrated and the solid was washed 12 times (to remove SDS) then particles were dried and ground. Composition of the inhibitor samples is summarised in Table 1.

Preparation of Paint Coatings

Paint coatings were layered on standard low-carbon, cold-rolled steel panels (RS type CRS, roughness; 25–65 micro-inches, complying with ASTM A1008.1010, A-109 and QQS-698 standards) were used as received from Q-Lab Ltd. PDIPs were dispersed by 20 min mortar grinding and milling in dissolved epoxy (at a polymer concentration of 50 wt.%).

Table 1. Elemental analysis determined component contents of PPy-deposited particles (wt.%) prepared at an initial molar ratio of iron(III)/pyrrole. Coulombic efficiency of PPy is derived from the voltammetry charging currents (on the average of five measurements) normalized according to the elemental analysis determined polymer contents of the PDIP samples based on nitrogen element

| Samples	PSS and SDS in the preparation mixtures (in wt.% and mol dm^{-3})	Types of MWCNTs in preparation mixtures and PDIPs (wt.%)	PPy in preparation mixtures (mol dm^{-3}) and PDIPs (wt.%), deposition yield of PPy (%)	Charging efficiency of PPy (%)
p1	-	-	0.10, (4.1) 83	3.7×10^{-2} ($\pm4\times10^{-3}$)
p2	-	-	0.10, (3.2) 64	3.3×10^{-2} ($\pm3\times10^{-3}$)
p3	2.34×10^{-2}, 3.5×10^{-3}	MWCNT-30, 1.28 (17.5)	0.10, (3.3) 29	3.7 ($\pm4\times10^{-1}$)
p4	1.35×10^{-2}, 1.7×10^{-3}	LS NC7000, 0.84 (12.4)	0.12, (5.4) 42	3.9 ($\pm4\times10^{-1}$)
p5	2.21×10^{-2}, 2.1×10^{-3}	LS NC7000, 0.10 (1.6)	0.10, (7.1) 61	1.8 ($\pm2\times10^{-1}$)
p6	2.64×10^{-2}, 2.1×10^{-3}	HS NC7000, 0.20 (3.2)	0.10, (5.2) 40	1.7 ($\pm2\times10^{-1}$)
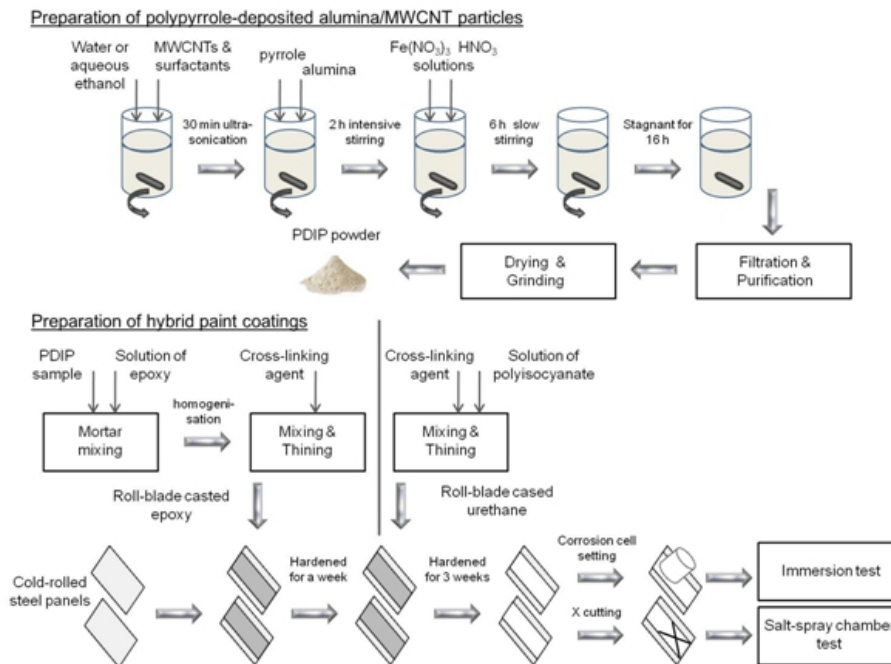
Figure 1. Representation of preparation procedures of the polypyrrole deposited alumina/multi-walled carbon nanotube particles and paint coatings.

Table 2. Composition of cured epoxy paint coatings in weight (wt.%) and volume fraction (φ), where hybrid C1–C6 contained PPy-deposited alumina/MWCNT particles at 3.21 wt.%

Coatings	PDIPs	PPy (φ) in the primer	PPy (φ) in epoxy resin	MWCNT (φ) in the primer	MWCNT (φ) in epoxy resin	Zinc
E	-	-	-	-	-	-
Z	-	-	-	-	-	90
ZA	-	-	-	-	-	70
C1	p1	0.133 (3.5×10^{-3})	0.456 (4.8×10^{-3})	-	-	70
C2	p2	0.103 (2.7×10^{-3})	0.354 (3.8×10^{-3})	-	-	70
C3	p3	0.114 (3.0×10^{-3})	0.392 (4.2×10^{-3})	0.417 (7.1×10^{-3})	1.428 (9.8×10^{-3})	70
C4	p4	0.186 (4.9×10^{-3})	0.637 (6.8×10^{-3})	0.429 (5.0×10^{-3})	1.472 (7.0×10^{-3})	70
C5	p5	0.242 (6.4×10^{-3})	0.830 (8.8×10^{-3})	0.056 (7.0×10^{-4})	0.191 (9.0×10^{-4})	70
C6	p6	0.175 (4.6×10^{-3})	0.600 (6.4×10^{-3})	0.111 (1.3×10^{-3})	0.381 (1.8×10^{-3})	70

The organic solvent was composed of 80:10:10 volume% of xylene (Fluka), 1-methoxy-2-propanol (Fluka) and 2-butanon (Aldrich). Suspensions of PDIPs were mixed with component A – stabilized zinc-rich masterbatch (HZO Farbenzinkstaub, Norzinco GmbH) in epoxy (Epoxidharz CHS141, bisphenol-A epoxy resin, Prochema). Component B – poly(amido amine) cross-linking agent (Durepoxy H15VP, USNER) was added to the suspensions, stirred to homogenize and diluted to get desired wet-concentration. Primer coatings were roll-blade casted on steel panels in 90 μm wet thickness (35±5 μm dry

thickness) and let cure for a week at room temperature. Top-coatings were layered on hardened epoxy in an overall wet thickness of 120 μm (80±5 μm dry thickness) with Macrynal SM 2810/75BAC hydroxyacrylic resin (CYTEC Industries Inc.) cured with aliphatic polyisocyanate resin: hexamethylene diisocyanate (Desmodur® N75MPA/X, Bayer Material-Science LLC) which was dissolved in the mixture of n-butyl acetate, xylene and isobutanol (2:2:1). Coatings were let dry and cure for three weeks at room temperature. Scribes were made by a blade as X-cuts.

Schematic representation of preparation of PDIPs and hybrid paint coatings are illustrated in Figure 1. In addition, Table 2 summarizes the composition of paint coatings.

CHARACTERIZATION OF POLYPYRROLE DEPOSITED ALUMINA/MWCNT PARTICLES

Elemental Analysis

Elemental analysis was performed by a vario EL *III* micro and macro CHNOS elemental analyzer (Elementar Analysensysteme GmbH, Germany) with about 4 mg sample.

Electrokinetic Potential

Zeta-potential characterization of the LS and HS NC7000 nanotube samples were performed in water by Malvern Zetasizer Nano ZS equipment, at dispersed phase concentration of 4×10^{-2}. Electrophoretic mobility of the particles was measured by Laser Doppler Velocimetry then Henry's equation was used to determine electrokinetic potentials based on the Smoluchowski approximation. The values of density (2300 kg m^{-3}) and refractive index (2.000) were used for MWCNTs, whereas refractive index (1.330), density (998.21 kg m^{-3}) and dynamic viscosity (1.002 Pas, at $20\,^{\circ}$C) of water were used for calculations.

Table 3. Volume fraction (φ) of the rheology investigated dispersions of the nano-particles suspended in dissolved alkyd resin at solid contents of 3.846 wt.%. Thixotropy index and yield stress determined by constant rate and force mode measurements are summarised

Particles	Alumina (φ)	PPy (φ)	MWCNT (φ)	Thixotropy (Pa s–1)	σ (Pa)
alumina	1.67×10^{-2}	-	-	1535	~0.5
p1	1.60×10^{-2}	1.63×10^{-3}	-	5024	9.7
p2	1.62×10^{-2}	1.27×10^{-3}	-	34591	3.4
p3	1.21×10^{-2}	1.40×10^{-3}	3.30×10^{-3}	634615	6.4
p4	1.31×10^{-2}	2.28×10^{-3}	2.34×10^{-3}	4340	1.5
p5	1.45×10^{-2}	2.96×10^{-3}	3.0×10^{-4}	72864	1.3
p6	1.44×10^{-2}	2.14×10^{-3}	6.0×10^{-4}	81720	18.6

Measurements indicated electrokinetic potentials of –24.7 and –31.4 mV of the low and the highly sulfonated nanotube samples at pH of 6.

Transmission Electron Microscopy

PDIP samples were crushed under ethanol and deposited onto copper grids covered by carbon supporting films. Transmission electron microscopy (TEM) data were acquired with a FEI MORGAGNI 268(D) microscope (FEI Co., The Netherlands) operated at 100 kV, with tungsten filament (top-entry; point-resolution = 0.5 nm).

Rheology

Measurements were done by a HAAKE RheoSress RS1 rotational rheometer (Thermo Fisher Scientific Inc., USA) equipped with a cone/plate sensor (2° angle, Ø 35 mm) used at a temperature of 25±0.3 °C. After three days swelling, PDIPs were dispersed by half an hour mortar grinding in of n-butanol and xylene (7:93) dissolved alkyd resin (distilled tall oil, SYLVATAL™ 25/30LT, Arizona Chemical, Gersthofen, Germany). Composition of the colloid mixtures are presented in Table 3.

Fourier-Transform Infrared Spectroscopy

PPy structure in $p1$–$p6$ PDIP samples was investigated by Fourier transform infrared (FTIR) spectroscopy using a Varian Scimitar 2000 FT-IR spectrometer (Agilent Technologies, Inc., USA) equipped with a broadband Mercury Cadmium Telluride (MCT) detector and a 'Golden Gate' attenuated total reflection (ATR) unit with diamond ATR element. 128 scans were co-added with a spectral resolution of 4 cm^{-1}. All spectra were ATR corrected using the Varian Resolution Pro 4.0 spectral handling software package.

Cyclic Voltammetry

Three-electrode cell configuration was applied for the electrochemical measurements. A platinum spiral ($A \approx 13$ cm^2) and saturated calomel electrode (SCE) were used as counter and reference electrodes, respectively. A platinum disc working electrode (diameter of 13 mm) was incorporated in a Teflon tube. Pressed pellets of PDIPs were attached to the working electrode by a Teflon bracket and wetted with 0.1 M acetonitrile solution of sodium perchlorate (Aldrich) used as electrolyte for the measurements. PPy contents of the pellets were reduced at –0.4 V for 30 min, then voltammetry scanning was performed at a rate of 10 mV s^{-1}. Current transients are normalized to unit mass of the PDIPs and the surface of working electrode. Prior to repeatability of the measurements and to avoid limitations in ionic mass transport, around 0.15 g of the samples was pressed with a maximum pressure of 250 kg cm^{-2}. Half an hour dwell-time preceded voltammetry investigation to ensure proper wetting and swelling of the sample pellets.

CHARACTERIZATION OF PAINT COATINGS

Electrochemical Impedance Spectroscopy

A platinum spiral, SCE and glass-tube-fitted paint coatings covered steel panels (A=5.3 cm^2) were used as counter, reference and working electrodes, respectively. The

electrochemical cell and the Zahner IM6eX potentiostat–frequency analyzer (Zahner-elektrik GmbH and Co., Germany) were placed into two grounded Faraday cages wired to each other. OCPs were measured in an open cell configuration. Then impedance measurements were carried out in the frequency range of 10 kHz and 20 mHz applying 20 mV sinusoidal perturbation according to the investigation principles of high resistance paint coatings [39].

Radio-Frequency Glow-Discharge Optical-Emission-Spectroscopy

RF-GD-OES analysis was started with sample preparation including the removal of

urethane top coat by gentle polishing, leaving the epoxy primer intact (in a 40 μm thickness).

Elemental depth profiling experiments were performed using a GD–Profiler 2™ radio-frequency glow-discharge optical-emission-spectrometer (RF-GD-OES) instrument (HORIBA Jobin Yvon S.A.S., France) equipped with a Paschen–Runge type polychromator (with 46 channels) optical system (focus distance: 0.50 m, diffraction grate: 2400 mm^{-1}, optical resolution: 18–25 pm) and a Cherny–Turner type monochromator (HR640, focus distance: 0.64 m) kept under nitrogen. Sample area was investigated under argon atmosphere at constant pressure of 500 Pa. Prior to high sensitivity detection of the corrosive analytes and coating elements, sputtering was performed at constant power (50 W) with voltage settings for the module (8.5 V) and the phase (3.0 V). Flushing time was 20 s at radio frequency plasma excitation of 13.56 MHz with an anode diameter of 4 mm. Depth profile data are presented over 40 μm of the epoxy primer coatings with an additional 20 μm sputtered crater in the steel substrates on average.

CHARACTERIZATION OF IMMERSION TESTED COLD-ROLLED STEEL SPECIMENS

X–Ray Photoelectron Spectroscopy

Immersion tested paint coatings on the steel panels were removed by three times of 5 min ultrasonication in the mixture of dichloromethane, methanol, toluene and tetrahydrofurane (6:1:1:1). XPS spectra were recorded from the steel surface on a Kratos XSAM 800 spectrometer operated at fixed analyzer transmission mode using Mg K$\alpha_{1,2}$ (1253.6 eV) excitation. Pressure of analysis chamber was lower than 1×10^{-7} Pa. Wide scan spectra were recorded in the 100–1300 eV kinetic energy range, applying pass-energy (80 eV) in 0.5 eV steps with 0.5 s dwell time. High-resolution spectra of characteristic photoelectron lines of constituent elements, and the C1s region for carbon-containing layers were recorded at pass-energy (40 eV) by 0.1 eV steps with 1 s dwell time. Chemical states of the constituents were determined by XPS database [40,41]. Kratos Vision 2000 software was used for quantifications with experimentally determined sensitivity factors. Omicron EA 125 type electron-spectrometer was employed with an excitation energy of AlKα (1486.6 eV) in the fixed analyzer transmission mode. Regions of interest were analyzed with the pass energy of

30 eV. CasaXPS [42] was applied to fit measured data and XPSMultiQuant [43,44] used for quantitative evaluation presuming homogeneous depth distribution of each component. Spectra were referenced to the energy of C1s line of polymeric or hydrocarbon type adventitious carbon set at 285.0 eV binding energy, and if it was applicable to the Fermi edge (0.0 eV binding energy) of the iron substrate.

Immersion and Salt-Spray Chamber Corrosion Tests

Immersion tests were carried out for 254 days with 1 M sodium chloride solution at room temperature, changing the electrolyte in a 42 day period. Corrosion tests were performed by a spray/prohesion/humidity cabinet (SF/MP/AB100, C+W Specialist Equipment Ltd., UK) installed with a Jun-Air (OF302, Gast Manufacturing Inc., USA) oil-free compressor. The 45 min cycles were divided into two phases. In the first 25 min, samples were exposed to salt fog combined with prohesion. Dosage rate of the sodium chloride solution (5 wt.%) was at 7 cm^3 min^{-1}. Temperature of the chamber was set to 35 ºC and the salt solution was heat up to 45±3 ºC. In the second phase, the temperature was held at 35 ºC for 20 min without application of salt mist. Test cycles were repeated for 142 days.

RESULTS AND DISCUSSION

Investigation of Ppy-Deposited Alumina/Mwcnt Particles

Transmission Electron Microscopy

Compared to the unmodified alumina shown in Figure 2a, enhanced dispersity of the water-solvent-prepared *p1* sample presented in Figure 2b was experienced when it was casted from polar protic solvent like ethanol. At higher resolution, the PPy-deposition caused coalescence of low number of the modified alumina particles at nano-scale is observed and pointed by arrow A on the microscopy image of Figure 2c. On the other hand, bridging type aggregation resulted in extensive, various sub-micron-scale aggregation of the PPy modified particles, signed by arrow B and C in the image. The thin layer of nearly uniform PPy coverage on the nano-size alumina carrier was also seen. In contrast, the aqueous-ethanol-solvent-prepared *p2* presented in Figure 2d exhibited partially globular polymer structure within the range of 30–70 nm with high micro-scale dispersity.
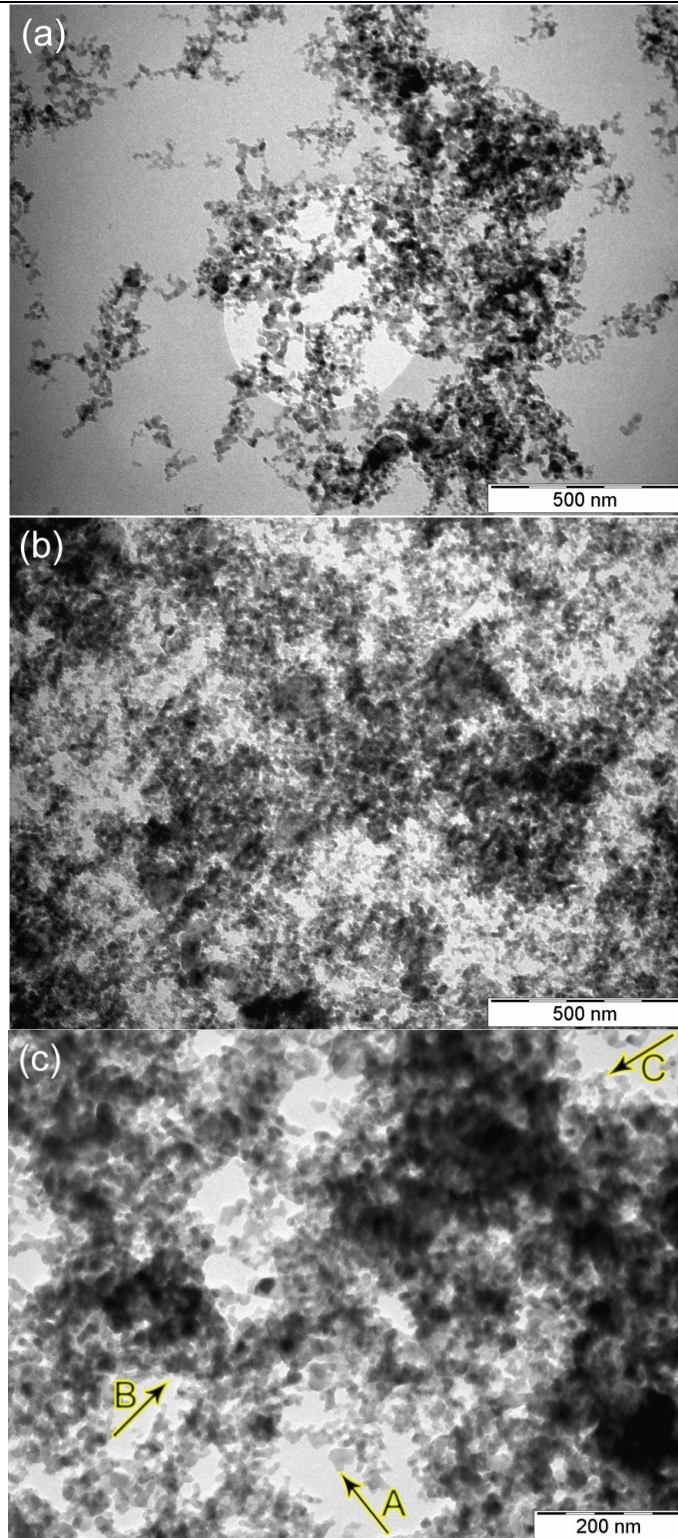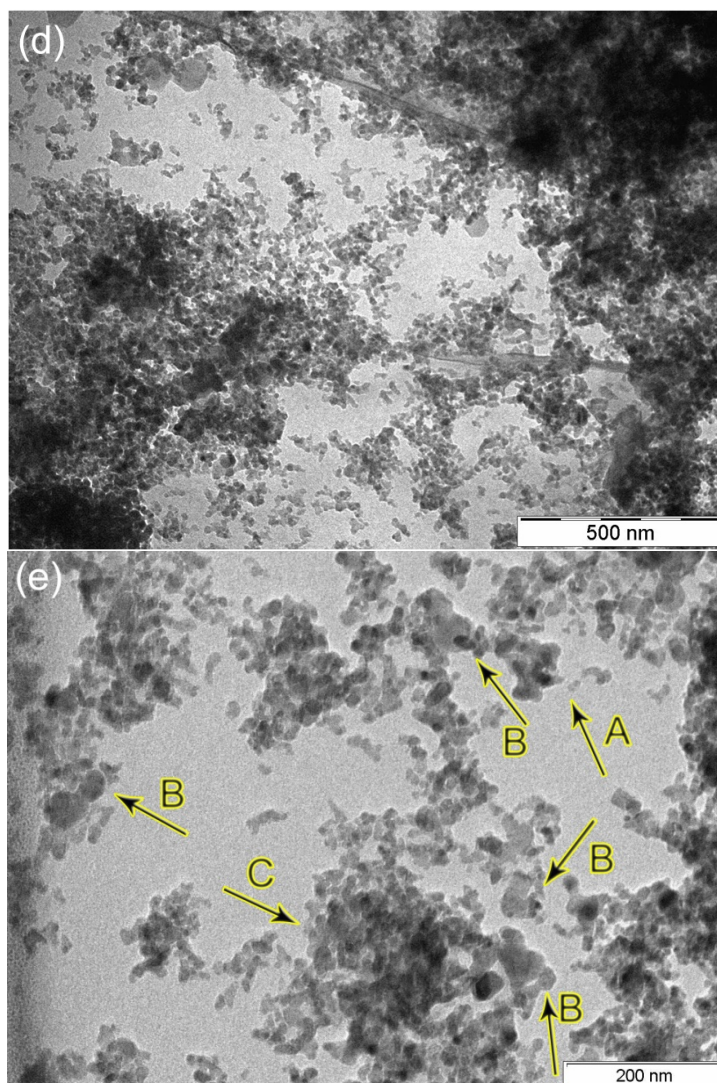
Figure 2. TEM images of (a) the nano-size boehmite alumina and the PPy-deposited alumina inhibitor particles: (b and c) *p1* prepared in water and (d and e) *p2* in aqueous ethanol.

Observations revealed the all around surface coverage of alumina by PPy as it is seen in Figure 2e.

The almost homodispersed sub-micron-scale structure of the *p2* contained individually dispersed PPy-modified particles in minor quantity (signed by arrow A) besides the majority of polymer coalescence caused moderately aggregated particles (noted by arrow B) and the 100 nm size agglomerated chunks (noted by arrow C). Increased dispersity of the PPy-deposited alumina is a result of homopolymer modification (organophilic modifier ensuring a certain range of entropy hindrance based steric repulsion) causing 'dispersant-effect' to prevent aggregation of the alumina carrier thereby supporting sufficient stabilization of highly dispersed composite systems. However, the moderate level of coalescence and polymer bridging type loose aggregation of the particles were manifested in both samples, according to

the imperfect deposition and incomplete polymer surface coverage. Nonetheless, bridging type aggregation should be easily overcome by agitation and applied strain or shear-stress.

Figure 3a depicts the polyelectrolyte modified nanotube embedded *p3* sample indicating almost homogeneous sub-micron structure with perfect random distribution of the PPy-modified alumina around the disentangled nanotubes. This is a result of the application of PSS polyelectrolyte and the SDS surfactant ensured high exfoliation of the nanotubes in the preparation mixture. Nonetheless, the more pronounced coalescence and bridging aggregation of the modified alumina were also observed which was resulted by the co-deposition of oppositely charged polymers, i.e. PPy with its PSS dopant. On the other hand, a markedly improved quality of PPy deposition is observed on alumina with a nearly complete polymer-film formation on the modified nanotubes. Figure 3b shows completely coherent microstructure of the modified carriers in *p4* containing large amount of PPy on alumina and the low functionalized NC7000 nanotubes.
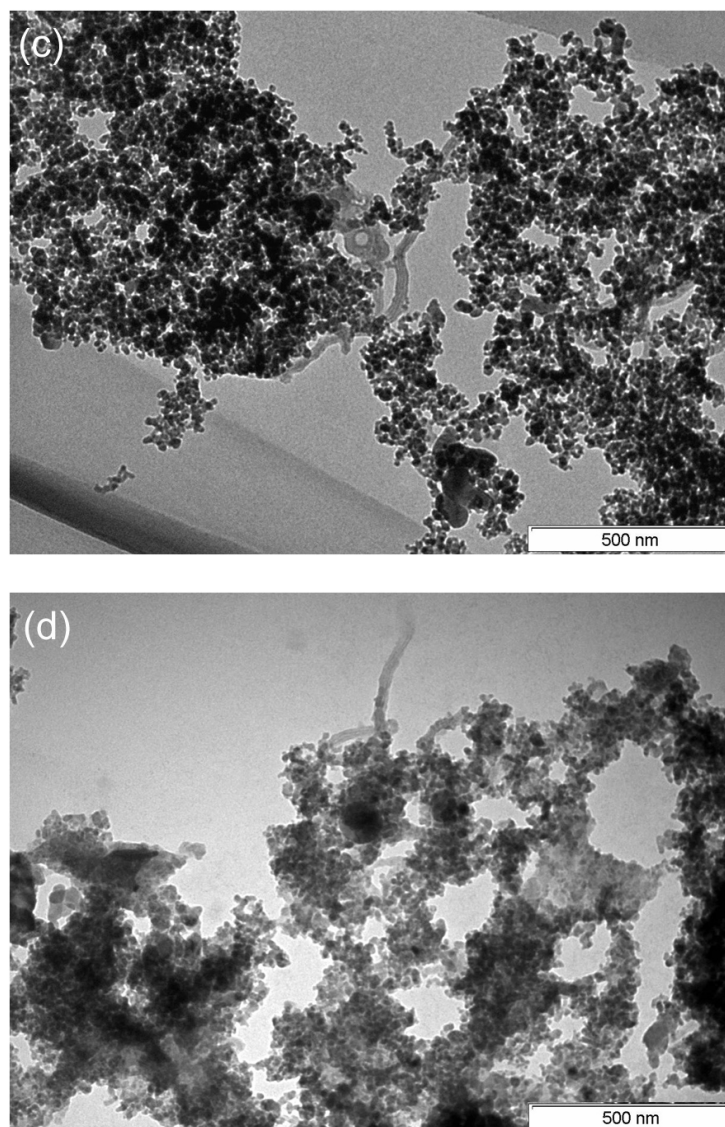

500 nm

500 nm
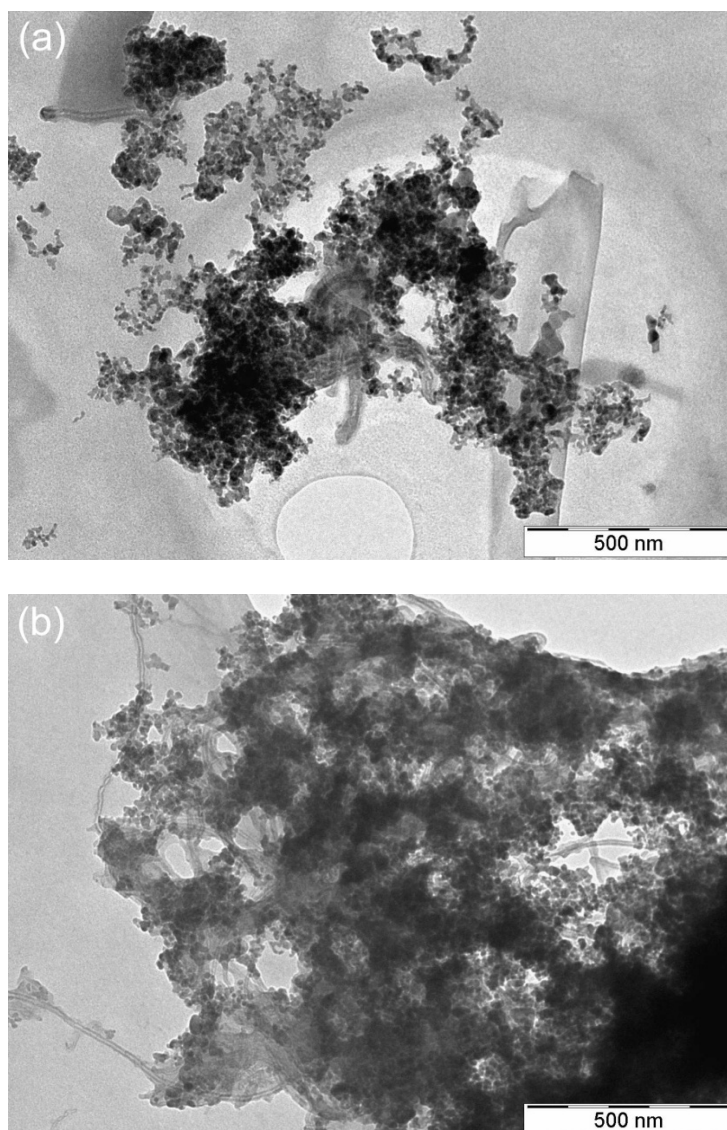
Figure 3. TEM images of the nanotube-embedded inhibitor particles embedded with: (a) *p3* PSS-modified MWCNT, (b and c) *p4* and *p5* low sulfonated MWCNT and (d) *p6* highly sulfonated MWCNT.

This sample indicated massive coalescence type aggregation of the modified particles. However, beyond the homogeneous micro-scale distribution of the carriers, the entire nanotube surface was coated with PPy, entailing in emerge of a more uniform properties of the inhibitor particles. The large amount of PPy and the polyelectrolyte modified small quantity of nanotubes embedded *p5* sample presented in Figure 3c exhibited voluminous nanotube-supported filaments with profound polymer bridging and moderate coalescence aggregation of the particles. Positive interparticle interactions within the bulky filaments rely on the even distribution of thin film co-deposited PPy and PSS on the carriers. Oxidative etching and sulfonate functionalization provided acidic character to the nanotube surface, contributing disentanglements and the formation of homogeneous PPy coverage along with

the polyelectrolyte adsorption assisted PPy-anchoring on alumina. In the case of *p6* sample depicted in Figure 3d, homogeneous polymer coverage was obtained both on the alumina and the nanotube carriers. However, the intense coalescence related aggregation of the particles was caused by the effective co-deposition of increased relative amounts of the polymers (Table 1) taking place through primary adsorption of the negatively charged PSS and SDS on alumina with a subsequent anchoring of the oxidative polymerized and positively charged PPy both on the on alumina and the functionalized nanotubes. This procedure has lead to massive coalescence and interparticle bridging of the particles with a strongly flocculated microstructure based on the closely interacted complexes by the synergistic role of 'double flocculants'. Otherwise, beyond the distribution of sulfonated nanotubes in *p4–p6*, dispersity of the PPy-modified particles was found experimentally not comparable to *p1* and *p2,* despite the reversible dispersibility of such types of aggregation and flocculation. Hence, there is a compromise in the overall dispersity when nanotubes are incorporated along with other types of nano-size carriers to form such intimate structures. The preparation routine to obtain *p2* involved using ethanol (13 vol.%) to stabilize the sol of freely dispersed alumina by varying the polarity of dispersant [45] and to assist the formation of dense polymer structure by lowering surface tension of the solvent and increasing the solvation of PPy. Despite the slower polymerization rate and lower deposition yield of PPy, this method was applied because of the increased solubilizing ability allowed the formation of globular polymer structure as it was observed in *p4–p6*. The amount of PPy was set to limit the thickness of superficial polymer film in less than 20 nm on average to minimize the occupied volume in paint dispersions.

The hardship to synthesize high performance anodic inhibitor particles, e.g. fully covered alumina with thin and compact PPy layer, arises from the fact that pyrrole does not adsorb on alumina in moderately solubilizing mixtures and adsolubilized poorly upon the application of SDS. Furthermore, pyrrole may decrease the adsorption ability of SDS on alumina (atypical behaviour) [46]. Thus, beyond the necessity of using SDS and PSS to ensure highly dispersed colloids in order to obtain acceptable degree of nanotube distribution in the PDIPs, PSS was used as an adsorption promoter and immobile complexing polymer to facilitate PPy deposition. However, the use of ethanol as co-solvent should be avoided in that case because of the presence of polyelectrolyte and ionic surfactant. SDS surfactant as a high affinity competitive adsorbing anion assisted well the early stage of PPy deposition on alumina via self-assembly mechanism featured 'Region II' admicelle type solloid adsorption with the formation of interfacial colloidal aggregates through charging and growth [47].

Rheology

Rheology characterization of dispersions of the inhibitor particles was performed to investigate solid-particle-interactions which depend on the concentration, dispersity, extent of interacting surface area and interfacial chemical nature of the filler phase, altogether governing the interfacial bonding with the matrix. Aspect ratio (P) of rod-like particles defined as $P \approx L/D$ (where L and D are the length and diameter) highly affects the viscoelastic behaviour of dispersions [48]. In our case, this was around 100 for both types of the nanotubes with ~20 and 50 nm diameters, on average. In the coatings of *C3* and *C4,* volume fraction of the nanotubes in the epoxy resin reached geometrical semi-dilute range (higher

than 5×10^{-3}, Table 2). Similarly, nanotube volume fractions were around that critical value in the rheology tested dispersions of the *p3* and *p4* PDIP samples (summarised in Table 3), at the same solid particle contents of 3.846 wt.%. On the other hand, dilute regime was valid for the *C5–C6* coatings and the rheology examined dispersions of *p5–p6* samples where volume fractions of the anisotropic particles remained under 5×10^{-3} (determined by the ratio of 2(D/4L)) [49]. However, the contents of alumina supported PPy along the part of the nanotube supported polymer in the epoxy resin of all hybrid paint coatings were around the threshold of geometrical semi-dilute range. This is because of the nano-size dimension of the particles related significantly decreased range of geometrical percolation, apart from the additional beneficial effects of the inhomogeneous particle distribution such as aggregation and flocculation of the alumina supported PPy causing lowered rheological and electrical percolation thresholds. Hence, explicit interaction of the nanotubes and their filaments are expected to be negligible in the *C5* and *C6,* whereas regarded as a long-range interaction in the semi-dilute type *C3* and *C4* paint coatings. According to the scope of this investigation, basic rheology study was performed to reveal the microstructure and interaction of the inhibitor particles. To draw appropriate conclusion about the corrosion resistivity of the *C1–C6* coatings containing various types of functional particles, solid contents of the rheology tested dispersions were chosen around the lower range of corrosion tested paint formulations.

To compare flow behaviour of the dispersions of the inhibitor particles, dissolved alkyd resin was also characterized. Almost ideal Newtonian flow behaviour of dissolved alkyd polymer and its dispersion with bare alumina was reflected by the wide-frequency range invariant complex viscosity, linear ramp of storage and loss moduli as well as the little changes in the phase angle (Figure 4a). Viscous flow character of the dispersion is associated with the absence of coherent microstructure.

High surface/volume ratio of the alumina is accounted for the increased dynamic viscosity of the dispersion at low solid content as a result of the high volume exclusion effect of the nano-size filler. Such character changed enormously by some nm thick water-solvent-prepared PPy layer was deposited on alumina and dispersed at the same solid concentration as bare alumina.

Figure 4. Frequency sweep type dynamic measurements of (a) dissolved alkyd resin, alkyd dispersion of boehmite alumina, *p1* and *p2*, and the nanotube-embedded (b) *p3–p6* particles at solid concentration of 3.846 wt.%, at a stress of 1 Pa.

The strong viscoelastic response of the pseudo-solid like colloid structure of *p1* dispersion is manifested by the entire frequency-range higher storage and lower loss moduli. Non-linear characteristic of the dispersion arranged by week attractive interparticle interaction through the dissolved polymer is reflected by the gradually decreasing complex viscosity, which is attributed to the shear-induced reorientation, nearly complete disruption of the highly associated three-dimensional system at high strain-rates.

In contrast, *p2* dispersion exhibited nearly strain-rate independent viscous characteristic (with higher loss and lower storage moduli due to inefficient load-transfer) which supports the suggestion of an absence of substantial interparticle interaction among the solid particles.

The lower scattered data of *p3–p6* dispersions confirm a good micro-scale dispersity of the nanotubes. However, in the co-dispersion of PPy-deposited alumina and MWCNT, profound effects of the various degree of aggregation, different distribution of the particles were experienced. Frequency-sweep test revealed strongly interacted colloid microstructure of *p3* dispersion by the intersecting storage and loss moduli at 10 Hz with the related elastic-viscous transition (critical stress-level) cross-over (Figure 4b). This was followed by steeply increasing moduli and complex viscosity indicating a more viscous flow behaviour (reflected by the high loss factor). The gradual ramp of higher loss and smaller storage moduli with the resultant high phase-angle reflect on less coherent structure of the *p4* dispersion, similarly to the considerably lower nanotube quantity comprised *p5* colloid sol. Coherent but less extensively associated flocculated colloid dispersion of *p6* were ascertained by the more elastic than viscous character (low phase shift) without a cross-over over the whole frequency range. These are associated with a strongly interacted, lower density nanotube-supported filamentous structure, which is in accordance with the TEM observations. Amplitude sweep measurement indicated stress-induced deterioration of the *p1* colloid structure with an elastic-viscous cross-over at 2.5 Pa (Figure 5a) which is a consequence of the increased interaction of the particles related to the thin film deposited PPy. On the other hand, the stress-ramp invariant viscous – fluid-like characteristic of *p2* sol containing partially globular PPy is connected to a far less associated and interacted three-dimensional structure. An elastic-viscous transition was noted to take place at 2 Pa in the *p3* dispersion with shear stress induced significant rupture of the colloid system (Figure 5b). No similar mechanical activation of the sol structure was observed in the *p4,* featuring predominantly viscous characteristic. Decreased complex viscosity of the *p5* sol (Figure 5c) compared to *p1–p2* is connected to the almost diminished inter-floc interactions among the nanotube-supported filaments arranged with aggregated PPy-modified alumina. Two-stages of the considerably high stress-activated elastic-viscous transition of the flocculated *p6* dispersion (reflected by the phase-shift at 5 Pa) confirm strong inter-floc association of the filaments in the colloid network.

Small hysteresis loop and the low monotonic shear-thinning at low strain rates (Figure 4a) suggest marginal structural viscosity of the dissolved alkyd matrix similarly to the alumina contained monodisperse system which manifested ignorable degree of association – floc formation of the randomly distributed particles. The Newtonian plateau of the viscosity over high strain-rates means a hydrodynamically controlled dispersion of the freely moving alumina particles. Aside from the slight bridging aggregation, the low stress required (Figure 6a) and the small thixotropy featured macroscopic flow behaviour of *p1* suspension (Table 3) are associated with rapid breakdown response and micro-scale association recovery of the thin-layer polymer deposited isotropic particles built highly interacted but less coherent medium-size flocs.

The apparent dynamic viscosity at high shear-rates was nearly the same as obtained with the bare alumina sol (Figure 6b), reflecting on an ignorable hydrodynamic effect of the interfacial PPy layer when complete collapse of the microgel flocs occurred.

The partially globular PPy contained suspension of *p2* indicated higher thixotropy as a result of the gradually disrupting, lower-site-number interacting, coherent larger size flocs with reorientation of the particles in the not fully collapsing micro-gels (even when durable straining performed at 300 s^{-1}).

Figure 5. Amplitude sweep type dynamic measurements of (a) dissolved alkyd resin, alkyd dispersion of *p1* and *p2*, and the nanotube-embedded (b) *p3–p6* particles at solid concentration of 3.846 wt.%, amplitude sweep at 1 Hz.

The lower pseudoplasticity with the largest stress-required straining (highest apparent dynamic viscosity) and the medium high yield-stress of the *p3* dispersion (Table 3) reveal altogether highly associated and coherent voluminous filaments built floc system featuring medium degree of three-dimensional inter-floc linkage. Strong thixotropy character of the gel-like dispersion is a result of the nanotube interactions around the rheology percolation related entanglement regime [50] allowing slower recovery of the gradually disrupted flocs. In contrast, at similar MWCNT volume fraction, pseudoplastic behaviour of the *p4* dispersion is connected to the fast response of preferential alignment–orientation of the nanotubes parallel to strain direction.

Figure 6. Steady measurements with upward (uw.) and downward (dw.) test results of (a) shear stress and (b) dynamic viscosity in the constant strain rate range of 0–300 s^{-1}, (c) constant force measurements in the stress range of 0–200 Pa, at solid concentration of 3.846 wt.%.

Consequently, the quite low apparent dynamic viscosity, thixotropy and yield-stress are attributed to a small density of poor inter-floc linkage, the absence of effective three-dimensional floc interaction, which is in accordance with the TEM observations. At lower PPy and nanotube contents, *p5* dispersion indicated increased dynamic viscosity, high thixotropy and very low yield-stress with pronounced shear-thinning effect which are connected to the lower extent of inter-floc linkage and stress-induced gradual attrition of the medium coherent flocs. This is a consequence of the double-flocculants modification resulted coalescence of the modified particles. The higher extent and strong aggregation of the particles and the related lower dispersity (effective volume fraction) of the system are revealed by the convergence of dynamic viscosity at high shear-rates where low hydrodynamic flow resistance was measured. Pronounced shear-thinning and the high dynamic viscosity of the *p6* dispersion are due to the extensively inter-linked microgel structure with strain-rate induced gradual but partial attrition of the nanotube-supported filamentous flocs. This was obviously accompanied by the release of entrapped dissolved polymer, leading to decreased effective hydrodynamic size of the remaining flocs at higher strain rates. The high yield-stress and thixotropy confirm a strongly inter-linked floc system, i.e. highly flocculated network based pseudo-solid-like structure featuring sluggish reorientation of disrupted flocs and aggregated modified particles.

Despite the poor packing effect and increased effective volume fraction of the rod-like particles [51,52], higher apparent viscosity was only measured to the *p6* dispersion over the entire strain-rate where volume fraction of the modified nanotubes was well under the

experimentally determined rheological percolation regime related entanglement threshold of the bare MWCNTs ($\sim 7 \times 10^{-3}$) [50]. This is because of the high dispersity and coherent three-dimensional structure of the inhibitor particles in spite of the decreased dispersibility of the polymer complex modified particles. On the other hand, the lack of ability to build up effective hydrogen bonding between alumina and the dispersant, leads to an inefficient enthalpy gain leveraging unpreferred entropy. Hence, hydrated alumina repels much of the lipophile matrix, so highly dispersed composite is not supported. Therefore, insignificant rheology control is connected to the weak van der Waals forces between the solid and the vehicle. On the other hand, PPy is in favour of interacting with the rheology tested lipohile alkyd and the paint formulated epoxy matrix via van der Waals forces and some hydrogen bonding. This is due to the similar Hansen solubility parameters of pyrrole ($\delta_{D,P,H}$ = 19.2, 7.4, 6.7) describing its dispersion, polar and hydrogen bonding ability with ethanol (15.8, 8.8, 19.4), epoxy ($\sim$15.6, 8, 4.6) and phenol (18, 5.9, 14.9) [53] segments contained structural polymers. Thus, layer type deposition of PPy resulted in increased interparticle interactions among the adjacent particles, which must be enhanced by the polar and hydrogen bonding ability of the polyelectrolyte and functionalized nanotubes. As a conclusion, basic rheology study was employed as representative macro-scale appraisal of the particle dispersions corroborating the suggestions made by TEM observations.

FT-Infrared Spectroscopy

The FTIR spectra obtained for the PDIP samples are depicted in Figure 7. The selected spectral region of 1800-1000 cm^{-1} implies the characteristic C–C/C=C and C–N stretching vibration bands of the polypyrrole ring [54,55]. The band at 1569 cm^{-1} in the spectra of water (*p1*) and aqueous-ethanol-prepared (*p2*) particles belongs to the combination of conjugated C–C and C=C stretching modes of the PPy rings.

This band, however, is blue-shifted compared to the one of the free-standing polymer situated at 1530 cm^{-1}. The bands at 1634 and 1340 cm^{-1} can be assigned to the deformations of protonated species like NH$_2^+$. For the *p2*, beside the strongest band at 1635 cm^{-1}, the medium intense N–H deformation band of terminal –NH$_2$ groups at 1110 cm^{-1} suggests a mediated oxidation – doping of the polymer, which might lead to partial cleavage of some pyrrole rings [56].

For the nanotube embedded samples (*p3–p6*), PSS bands were also present in the spectra (marked with asterisks in the figure). The in plane deformation bands of =C–H groups detected at 1294 and 1047 cm^{-1} are due to the greater PSS polyelectrolyte proportion in the *p3* and *p5* samples. Spectral effects of the SDS can be neglected because of the thorough consecutive washing process. There are marked differences in the typical spectral features of the PPy. The characteristic bands around 1560/1570, 1170 and 1050 cm^{-1} proved a good quality of the PPy in *p3–p6* without overoxidation, confirming an increased stability/chemical durability of the nanotube-supported PPy. Despite the strong spectral masking effect of the sulphoxide group, the relative high band intensities at 1170 cm^{-1} (N–C stretching of pyrrole rings) and 1050 cm^{-1} (=C–H inplane deformation) can be related to a compact PPy structure with increased electroactivity and electrical conductivity based on electron hopping near the N–C bond [57].

Figure 7. FTIR spectra of PDIP samples: water- and aqueous-ethanol-prepared PPy-deposited alumina particles (*p1* and *p2,* respectively), comprising PSS-modified MWCNT (*p3*), low sulfonated MWCNT (*p4* and *p5*) and highly sulfonated MWCNT (*p6*). Asterisks in the spectra indicate characteristic bands of PSS polyelectrolyte.

Suppressed δC–H deformations indicated by the bands at 1294 and 1047 cm^{-1} suggest stronger co-planar characteristic of the PPy segments throughout the polymer backbone. The relative high band intensities at 1170 cm^{-1} (C–N stretching) and 1038 cm^{-1} (=C–H inplane bending) in the spectrum of *p1*, *p3* and *p4* suggest a chain-like, co-planar PPy structure. For the low functionalized nanotube-alumina contained *p4* sample, PPy spectrum resembles to those of bare alumina supported polymer obtained in *p1* and *p2* samples. Hence, the spectrum suggests a more compact, mostly film-like PPy structure in *p4*. The broad band around 1330 cm^{-1} assigned to the N–H bending of NH$^+$ groups suggests a partially doped, protonated PPy. The suppressed C–N stretching and C–H bending intensities compared to the one of the conjugated C–C/C=C stretching of pyrrole rings point to the fact that the deposited polymer might mainly be in a three-dimensional structure. In the case of *p4*, reduced concentration of SDS and PSS allowed the formation of moderately protonated – doped PPy with medium degree of deposition. Hence, highly conductivity and electroactive inhibitor sample was obtained as it is clearly indicated by cyclic voltammetry.

Collective vibration of C=C/C–C inter and intra-rings appears at 1560/1570 cm^{-1} compared to 1530 cm^{-1} of the neat PPy. This blue shift can be explained by an enhanced electron delocalization in the polymer backbone [58] and was found to be higher for the sulfonated nanotube containing *p5–p6* samples (around 1575 cm^{-1}). The same blue-shift accompanied with the rising of a new band around 1220 cm^{-1} in the C–H and N–H in-plane deformation region is connected to the changes in the doped – protonated and base forms of PPy. The spectrum of *p6* PDIP containing highly sulfonated MWCNT and alumina supported PPy is somewhat different owing to the polymer partial interaction with the highly functionalised nanotubes and the complexing PSS polyelectrolyte. On the other hand, PPy content indicated film-like and globular character with the bands at 1160, 1570 cm^{-1} and the wide-range around 1350, 1660 cm^{-1}, respectively. Therefore, the high wavenumber of collective C–C/C=C vibrations at 1573 cm^{-1} together with the C–H/N–H in-plane deformation around 1210 cm^{-1} suggest the presence of a base form of the PPy. Hence, it is obvious that PPy is doped predominantly by the highly sulfonated nanotubes whereas alumina supported polymer could be complexed with small portion of PSS. The relative high band intensities at 1170 cm^{-1} (N–C stretching of pyrrole rings) and 1050 cm^{-1} (=C–H inplane deformation) detected in *p3* and *p4* are associated with compact polymer structure with increased electrical conductivity. In addition, the collective vibration of C=C/C–C inter and intra-rings at 1560/1570 cm^{-1} (compared to 1530 cm^{-1} of neat PPy). The blue shift associated with an enhanced electron delocalization in the backbone [67,68] is typical to the sulfonated MWCNT-embedded *p5* and *p6* (1575 cm^{-1}). These observations regarding the structure of the PDIP samples corroborate cyclic voltammetry results of increased conductivity and enhanced redox-activity of the nanotube-embedded inhibitor particles.

Cyclic Voltammetry

Electroactivity and conductivity are important properties having strong influence on the corrosion inhibition function of the PPy regardless it is used as stand-alone polymer films or carrier-supported forms in composite coatings.

Figure 8. Cyclic voltammograms of water- and aqueous-ethanol-prepared PPy-deposited alumina particles (*p1* and *p2*), with PSS-modified MWCNT content in *p3*, low sulfonated MWCNT in *p4* and *p5*, and highly sulfonated MWCNT in *p6*, referenced to the base current of platinum electrode. Sweep rate is 10 mV s^{-1}.

Taking into account that PPy contents of *p1* and *p2* (as conducting network) were around the percolation threshold [59], valuable coulombic efficiency of the samples was ascertained (Table 1) by the transient charging voltammetry currents which are presented in Figure 8.

Highly reversible current responses were exhibited, confirming moderate electrical conductivity and redox activity of the Ppy contents of the inhibitor particles.

Similar charging efficacy and the highly reversible current transient of the *p2* comprising lower amount of PPy, suggest an altogether increased mobility of charges in the conducting polymer network compared to *p1*. Current transient of the *p3* indicated medium degree of electrochemical reversibility with improved conductivity and redox ability which are related to the greater current response. The almost ideal resistance like voltammetry current response of the *p4* sample manifests enhanced reversibility of the PPy and charge mobility in the polymer backbone, which are due to the enhanced interaction between the PPy and the nanotubes based increased electrical conductivity of the modified particles. The highly dispersed but low amount of nanotube-incorporated strongly aggregated filamentous structure comprised less interlinked PPy network in *p5* allowed the evolution of relatively high current transients with medium fast kinetics related appropriate reversibility since moderate coulombic efficiency was obtained (containing greater amount of surfactant similarly to *p3*). The current image was also resulted by the greater specific polyelectrolyte content of *p5* which is responsible for the somewhat restrained mobility of the charges in PPy backbone. This is a consequence of the closely interacted complexes of the PPy and PSS molecules, allowing limited conjugation in the partially doped polymer network by the larger distortion and conformational adjustments of the Ppy segments. The current response related enhanced reversibility and improved charge mobility (despite the medium PPy and low nanotube contents) resulted in considerable coulombic efficiency of the PPy in the *p6* sample. This is connected to the highly interconnected, homogeneously distributed nanotube-supported, thin film deposited PPy network with closer interaction and efficient electron transfer between the nanotube carrier and the deposited PPy. Although, PPy charging efficiencies were around 4%, high electroactivity and the moderate electrical conductivity must contribute to the interaction of sacrificial zinc pigments. Increased efficiencies of the galvanic function of the hybrid paint coatings are expected based on the rheology indicated nanotube interactions at a certain solid concentration. Therefore, advanced galvanic protection function of the hybrids is expected to be comparable to the traditional type ZRPs.

INVESTIGATION OF IMMERSION TESTED ALKYD PAINT COATINGS AND STEEL SUBSTRATES

Open-Circuit Potential and Electrochemical Impedance Spectroscopy

The markedly fluctuated, positive polarized OCPs of the salt-solution tested pigment-free epoxy coated steel sample (*E*) are presented in Figure 9a. The measured impedance spectra shown in Figure 9b exhibited almost ideal capacitive behaviour up to 152 days, confirming the firm passive protective function, very low electrolytic conductivity of the coating. Then, the low rate of electrolyte infiltration was disclosed by the stabilized OCPs and the little increasing low-frequency phase-angle minimum in the impedance spectra. The positive mixed potentials suggest notable shrinkage in the area of anodic processes, giving evidence about the suppressed rate of iron dissolution. However, around 225 days the anodic polarization slowly decreased due to the acceleration of anodic processes at the steel surface. At the end of the immersion test, steel substrate was corrosion-free but the primer completely delaminated. Evaluation immersion test results are summarised in Table 4.

Table 4. Evaluation of hydrochloric acid solution tested paint coatings, corresponding to the EN ISO 4628-8:2005 standard

Coatings	Degree of blistering size and density	Degree of delamination	
E	1	1	complete
Z	2	2	severe
ZA	2	4	moderate
C1	1	3	none
C2	-	0	none
C3	-	0	none
C4	-	0	none
C5	-	0	none
C6	-	0	none

Figure 9. Open-circuit potentials (a) and electrochemical impedance spectra (Bode plots) of steel samples protected with paint coatings of (b) neat epoxy (*E*), (c) conventional type zinc-rich epoxy (*Z*), (d) zinc-rich epoxy with alumina (*ZA*), (e) *C1* and (f) *C2* hybrid paint coatings containing water- and aqueous-ethanol-prepared *p1* and *p2* particles, immersion tested with 1 M sodium chloride solution for 254 days.

The conventional type zinc-rich *Z* provided strong and remarkably durable cathodic polarization – thermodynamic immunization of the steel substrate for 127 days (Figure 9a)

which was in accordance with the intense sacrificial action of zinc pigments. In the meantime, deteriorating barrier profile of the coating was reflected by acquired EIS data featuring small and decreasing impedance moduli with high-frequency-range shifted breakpoint-frequencies depicted in Figure 9c. The notable drops in the impedance moduli measured at 38 and 172 days correlated with the deactivation and reactivation of cathodic galvanic function of the primer by the increasing and decreasing extent of electrolyte ingress. These processes were followed by moderate recoveries in the barrier nature around 73 and 200 days, which connected to the lessened electrolyte penetration and lower rate of dissolution of the accumulated zinc corrosion products. Evolved second time constant in the phase diagram is attributed to a greater double-layer capacitance. The interfacial galvanic cell at the steel surface is connected to severe deterioration and de-adhesion of the primer coating (containing partly heavily corroded metallic pigments) with its diminishing all around protective function. In this case, enhanced sacrificial function of zinc is propelled by the great deal of electrolyte infiltration and the possible high rate of oxygen reduction reaction (ORR) accompanied with the subsequent evolution of strongly alkaline milieu as well. Despite the severe delamination of coating *Z* which is in accordance with the severe oxidative degradation [60,61] and saponification of the epoxy binder, no corrosion spots were detected on the steel surface.

Except for a positive potential shift around 100 days (Figure 9a) followed by a short-term recovered barrier nature of the *ZA* (Figure 9d), steadily decreasing OCPs with the appearance of breakpoint-frequency and the high low-frequency phase-angle minimum measured until 73 days, suggest an altogether low efficiency galvanic function of the zinc-rich/alumina primer coating along with the steady electrolyte infiltration associated continuously degrading barrier behaviour which became pronounced from 127 days. Stable OCPs around –0.6 V vs. SCE are connected to steel corrosion whereas decreasing low-frequency impedance moduli with the migration of breakpoint- and saddle-frequencies towards the high-frequency domain unveiled gradually increasing electrolytic conductivity. At the end of immersion test, the coating was moderately blistered and slightly delaminated. The steel substrate was somewhat corroded with considerable quantity of precipitated zinc corrosion products on the surface. Consequently, paint coatings based on the composition of highly dispersed alumina and spherical zinc pigments at contents of 3.21 and 70 wt.% provides neither efficient galvanic nor firm barrier protective function to steel substrates against corrosion.

The similarly changing anodic shifted OCPs manifested generally low activation of the galvanic function of the *C1* and *C2* coatings (Figure 9a) by electrolyte ingress due to the firm barrier behaviour of the coatings. The latter is reflected by the high impedance moduli and the quite low phase-angle minimum in the low-frequency domain as it is shown in Figures 9e and f, allowing very limited electrolyte access into the primers and to the anodic pigments. Such nature of the coatings changed around 73 days when OCPs shifted cathodically coinciding with the lower impedance amplitudes and higher low-frequency-range phase-angle minimum associated increased electrolytic conductivity. The anodic polarized OCPs with improved capacitive features at 100 days denote effective recovery of the corrosion resistance of the coatings as a result of the accumulation of small amount of zinc corrosion products. The absence of valuable cathodic galvanic action of the hybrid primers is connected to the complex function of the highly dispersed PDIPs supporting lower extent of electrolyte ingress and inhibition of the sacrificial and self-corrosion of the anodic zinc pigments. During the second half time-period of the test, *C1* and *C2* coatings afforded stable corrosion prevention

which was noted by the ignorable changes in the OCPs and the impedance data giving evidence about the hindered electrolyte infiltration into the coatings. Apart from the small number and size of blisters on the surface of *C1* in conjunction with its moderate galvanic function and the osmosis propelled blistering, no de-adhesion or delamination of the hybrid paints and steel corrosion were experienced.

Within the first 50 days of immersion, the large amount of polyelectrolyte modified nanotubes contained coating *C3* manifested slow activation of its hybrid primer by the strong anodic polarized mixed potentials shown in Figure 10a with effective barrier functionality reflected by the impedance data presented in Figure 10b. Anodically shifted OCPs are caused by the shrinkage in the effective anodic surface and the inhibited sacrificial action of the zinc pigments, leading to comparable areas of the galvanic coupled anodic and cathodic reactions. The main reaction of oxygen reduction took place obviously both on the steel surface and zinc pigments along with the low intensity galvanic action of the primer, resulting in low potential gradient in the coating/steel interface. The little increased electrolyte penetration through the *C3* was marked by the cathodic shifted OCPs at 100 days which occurred 25 days later than in the case of *Z4*, *C1* and *C2* coatings. This was accompanied by an ignorable impedance modulus drop and insignificant increase in the low-frequency phase-angle minimum. However, the 50 days period of continuous activation of the *C3* and the more intense anodic action of its zinc content was followed by efficient pore-filling recovery. This was indicated by the stabilized positive OCPs and the more capacitive coating behaviour associated improved electrolytic barrier function which remained stable to the end of immersion test. All these features of the hybrid paints are mainly attributed to the beneficial action of the *p3* type anodic inhibitor particles having high dispersity and extensively interconnected microstructure with well conducting and redox active nanotube-supported PPy network in the epoxy vehicle.

The slightly lower electrolytic barrier nature of the low sulfonated nanotube contained coating *C4* was reflected by the insignificant cathodic polarization of the OCPs (Figure 10a) and the EIS data indicated breakpoint-frequency in the low frequency domain (Figure 10c). The evolution of negative polarized OCPs within the first 20 days reflects on moderate activation rate of the coating by the penetrating corrosive electrolyte. The following positive potential shift at 40 days coincided with the greater pore resistance connected enhanced barrier profile (more capacitive character) revealing fast recovery of the corrosion resistance of the *C4* resulted by the efficient accumulation of corrosion products.

This process took place repeatedly at a longer time-scale until 120 days when more stable passive protection function developed and remained stable to the end which was reflected by the slow negative polarization tendency in the OCPs and the unchanged impedance data.

Potential fluctuations and the greater ionic conductivity of the *C4* are resulted by the strongly aggregated and less interconnected microstructure of the *p4* particles in epoxy around the bulky zinc pigments.

Besides the negatively and positively shifted OCPs, impedance spectra presented in Figure 10d with the almost unchanged impedance parameters manifested gradual but an overall slightly increased ionic conductivity of the *C5* up to 172 days of immersion. Similarly to the *C4*, the low quantity of sulfonated nanotubes in *C5* with high relative amount of the polyelectrolyte indicated two–stages of electrolyte ingress related minor activation and blocking.

Figure 10. Open-circuit potentials (a) and electrochemical impedance spectra (Bode plots) of steel samples protected with hybrid paint coatings containing inhibitor particles embedded with (b) PSS-modified MWCNT (*C3*), low sulfonated MWCNT (*C4* and *C5*) and highly sulfonated MWCNT (*C6*), immersion tested with 1 M sodium chloride solution for 254 days.

The little increased pore-resistance is related to the corrosion resistance recovery of the *C5* occurred around 50 and 100 days. From 200 days, OCPs became more anodic as a result of the mixed potentials of the varied surface area related half electrode reactions connected to the suppressed zinc dissolution and the galvanic coupled ORRs on the steel surface. The improved barrier nature of the primer was noted by the continuously decreasing low-frequency phase-angle minimum. These changes are connected to the slow development of the long-term passive protection phase of the hybrid paints (similarly to the conventional ZRPs). The less anodically shifted potentials with firm barrier functionality of the coating are attributed to the lower inhibition of zinc corrosion at low extent of electrolyte penetration which was a consequence of the effect of the highly aggregated and least coherent microstructure of the *p5* particles in the epoxy resin.

In the case of coating *C6*, the frequently fluctuating anodically polarized OCPs measured in the first half of the immersion test were followed by cathodic polarization and stabilization of the mixed potentials (Figure 10a) as a consequence of the altered corrosion preventing behaviour of the coating. This was accompanied by the changing barrier nature of the hybrid primer coating between its activated and recovered forms signified by the migration of the breakpoint-frequency towards the high frequency domain and the increasing low-frequency phase-angle minimum in the impedance spectra shown in Figure 10e. Thus, the highly sulfonated nanotube-embedded *p6* sample with medium quantity of polyelectrolyte and the densely interconnected flocculated microstructure of the particles around the zinc pigments contributed to a less durable barrier functionality of the *C6* coating with higher zinc corrosion.

Radio-Frequency Glow-Discharge Optical Emission Spectroscopy

Hybrid paints were investigated by RF-GD-OES to draw sound conclusion about the electrolytic conductivity of the primer coatings based on the comparison of the composition of the initial and the immersion tested of paint coatings, detecting elements in ppm quantities by this high resolution depth-profiling technique. Changes in the quantities of corrosive species and coating elements are presented in relative intensities (normalized to the intensity of carbon) as a function of sputtered depth.

By this method, the EIS data suggested low ionic conductivity–permeability of the nano-size alumina contained zinc-rich *ZA* was confirmed detecting unchanged quantities of the corrosive species in the whole cross-section of the primer (Figures 11a and b). However, aside from the unaffected sum of the anions, the 6% increment in the oxygen content in the region of epoxy-steel surface suggest moderate barrier profile and the related low efficacy of the

intense sacrificial and self-corrosion of zinc (galvanic function of the primer). This must have been the result of the absence of any valuable corrosion inhibition of the zinc pigments which was available to hybrid coatings afforded by the PPy-modified inhibitor particles. Almost the same quantities of the corrosive analytes like sodium, potassium and chlorine were detected through the cross-section of epoxy primer in *C1* after the corrosion propagation (Figures 12a and b), corroborating the impedance data suggested largely hindered electrolyte ingress. Potassium concentration in the hybrid is estimated about 4.5×10^{-2} mol dm^{-3} and only little affected by the immersion test. Minor relative intensity changes of the coating elements are related to the cross-sectional and spatial fluctuations in the local pigment/binder contents. In contrast, sodium and potassium were detected in higher quantities in the solution-primer interface of the immersion tested *C2*, as it is shown in Figures 13a and b. As a result of the slow electrolyte infiltration, sodium and potassium accumulated in the epoxy at concentrations of 2×10^{-3} and 1×10^{-1} mol dm^{-3}, respectively. However, the unchanged chlorine concentration in *C2* suggests very low electrolytic conductivity of the hybrid primer to the anionic species. This reflects the ignorable effect of the *p2* type particles on the ionic permeability and the corrosion resistive character of such type of hybrid formulation. In addition, detected potassium in the epoxy near the solution interface is due to the some percentage of potassium impurity in the sodium chloride and the smaller hydrodynamic radius resulted higher mobility, faster diffusion and migration in the organic coatings [62].

Moreover, the greater oxygen content in the primer-steel interface (~20–40 μm) and the slightly increased quantities of the cationic species in the 0–20 μm depth-range hint on the viable cathodic–galvanic function of the *C2* hybrid.

Nonetheless, the nanotube contained hybrid coatings manifested more advanced passive protection functionalities which were revealed by the comparison of corrosive species. No remarkable accumulation of any corrosive analyte was found in the cross-section of the *C3* (Figures 14a and b) which is accordance with the impedance data suggested massive and stable barrier nature of the coating.
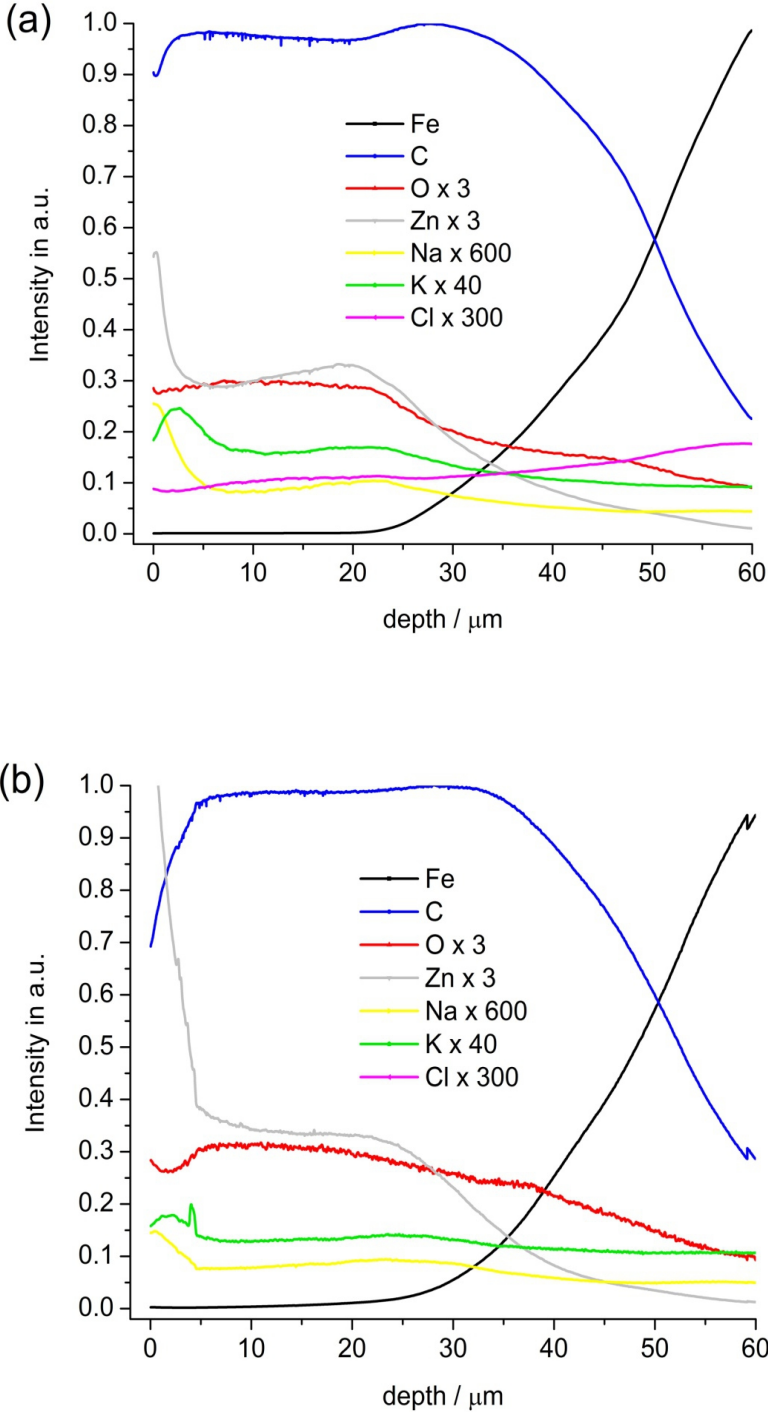
Figure 11. GD-OES depth profiled coating elements and corrosive analytes in the epoxy primer of *ZA:* (a) before and (b) after the 254 days of immersion test.
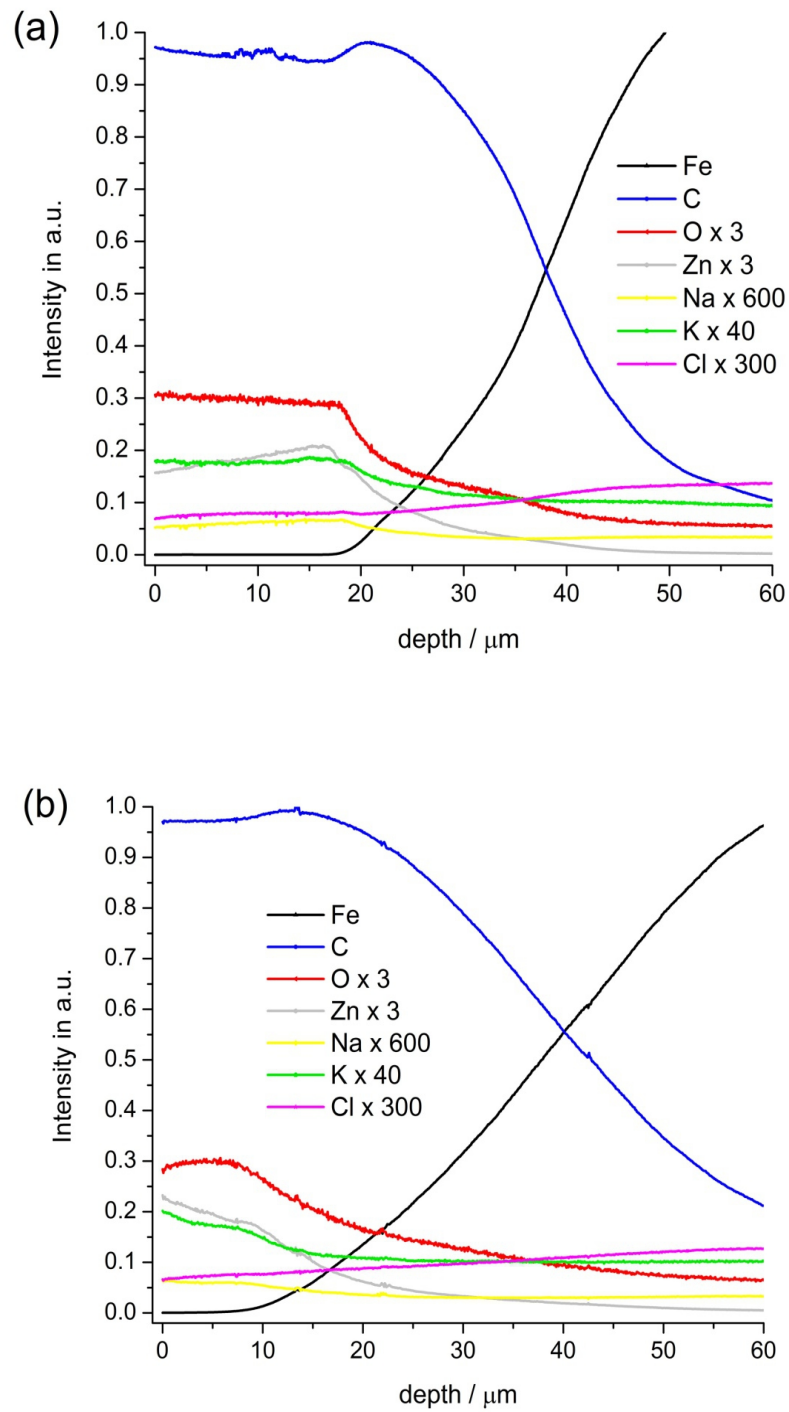
Figure 12. GD-OES depth profiled coating elements and corrosive analytes in the epoxy primer of *C1*: (a) before and (b) after the 254 days of immersion test.
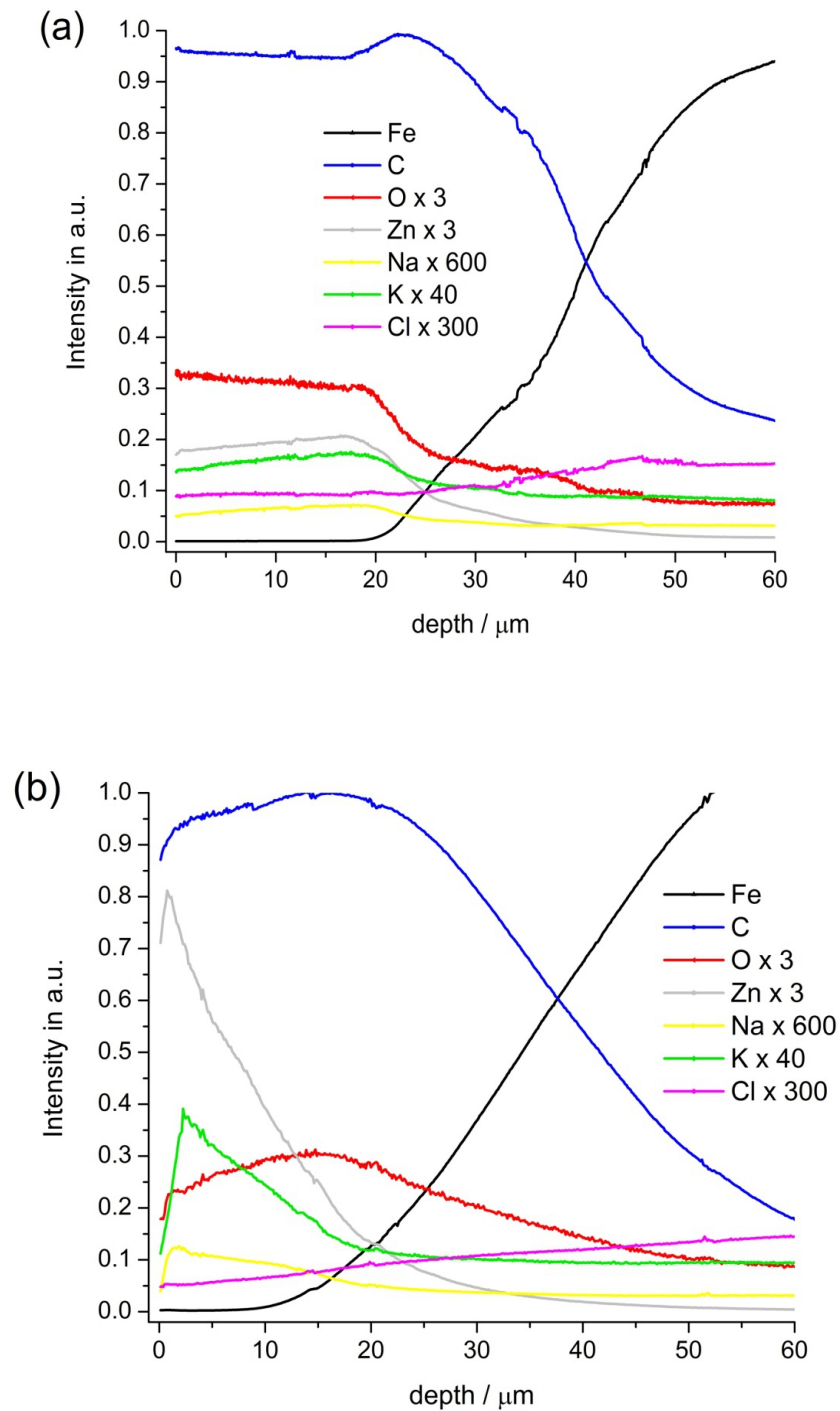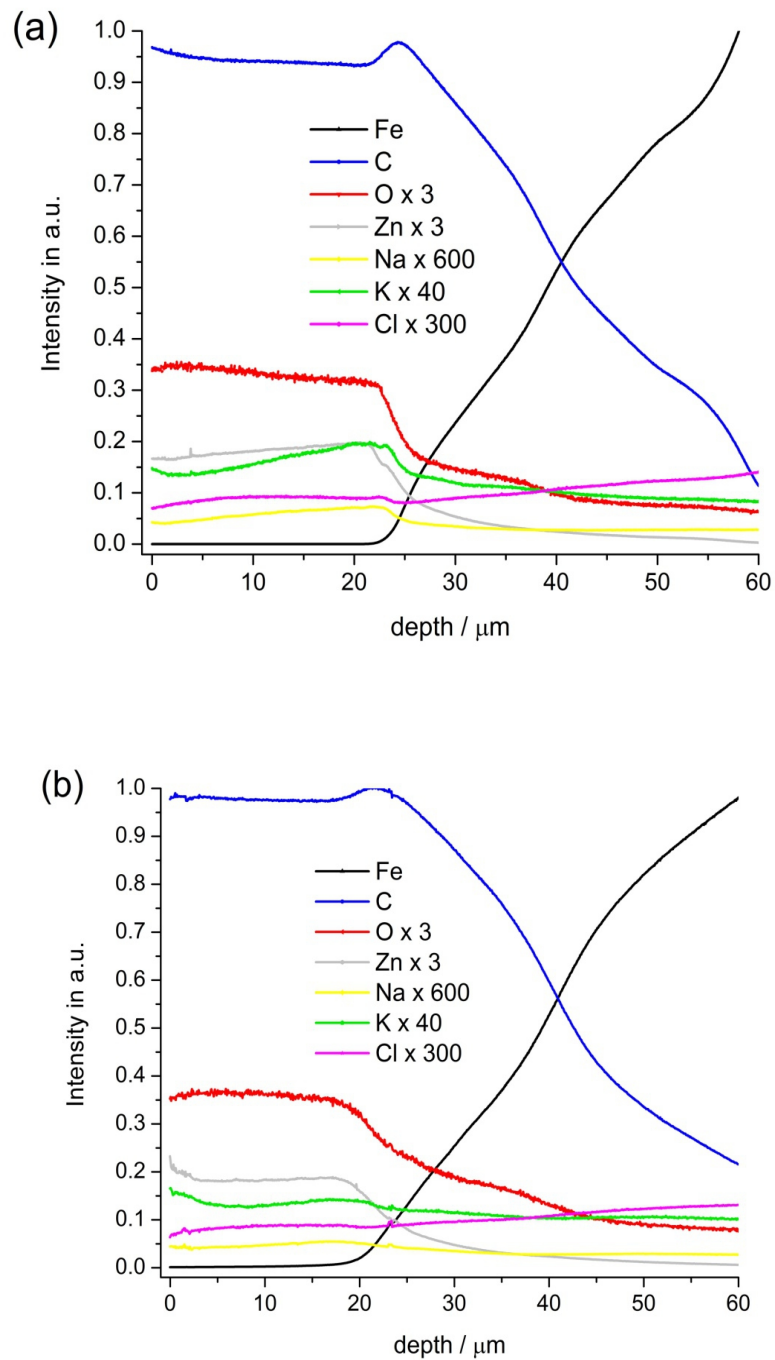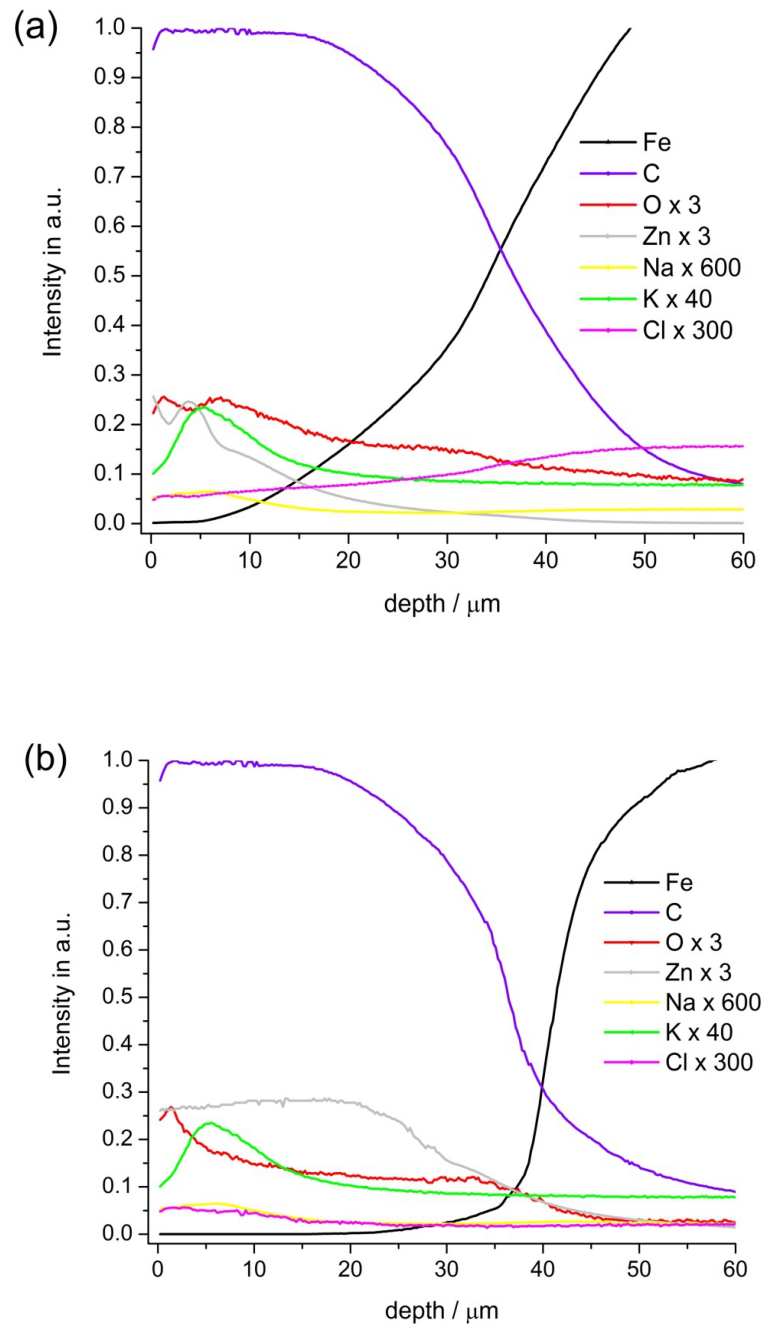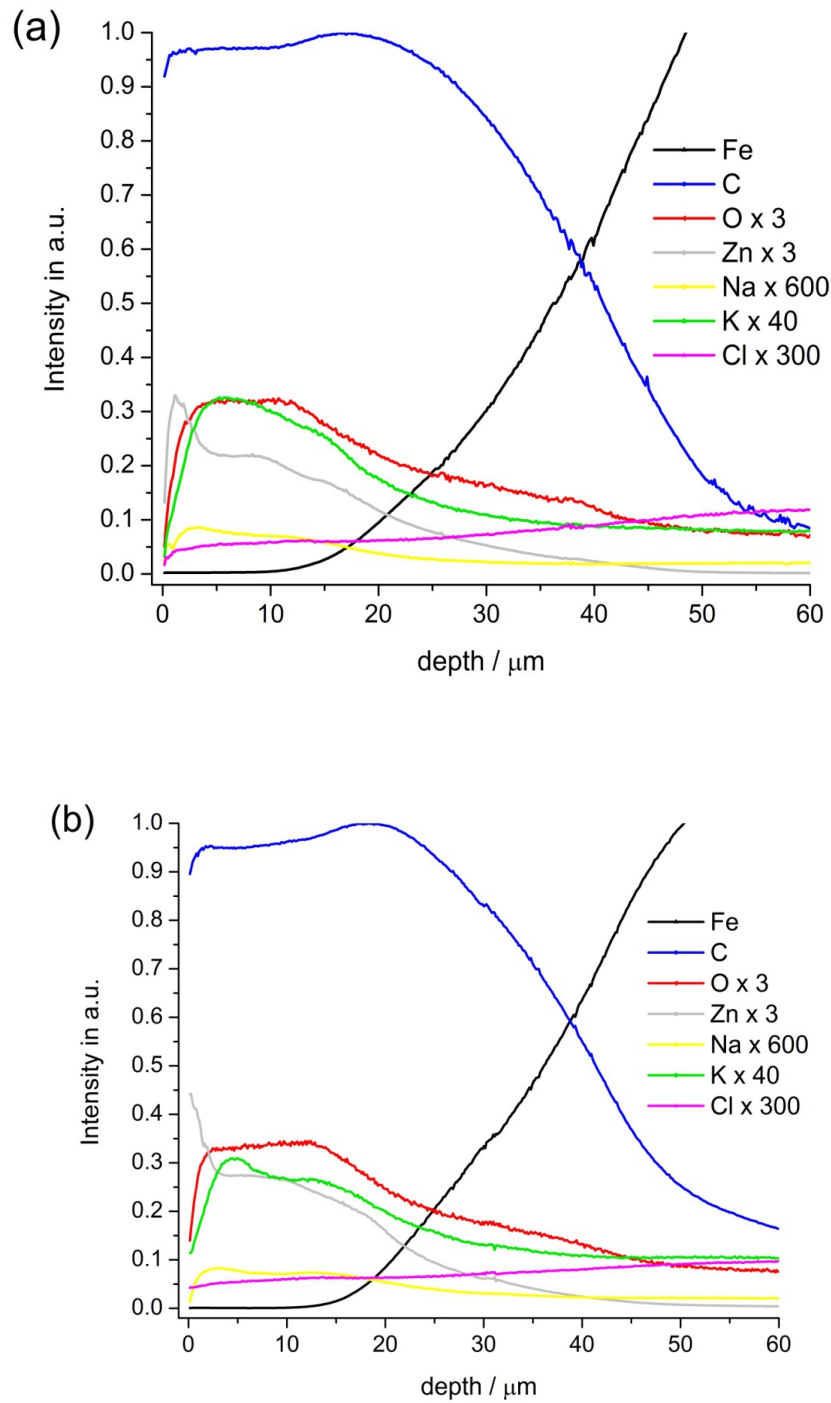
Figure 13. GD-OES depth profiled coating elements and corrosive analytes in the epoxy primer of *C2*: (a) before and (b) after the 254 days of immersion test.

Figure 14. GD-OES depth profiled coating elements and corrosive analytes in the epoxy primer of *C3*: (a) before and (b) after the 254 days of immersion test.
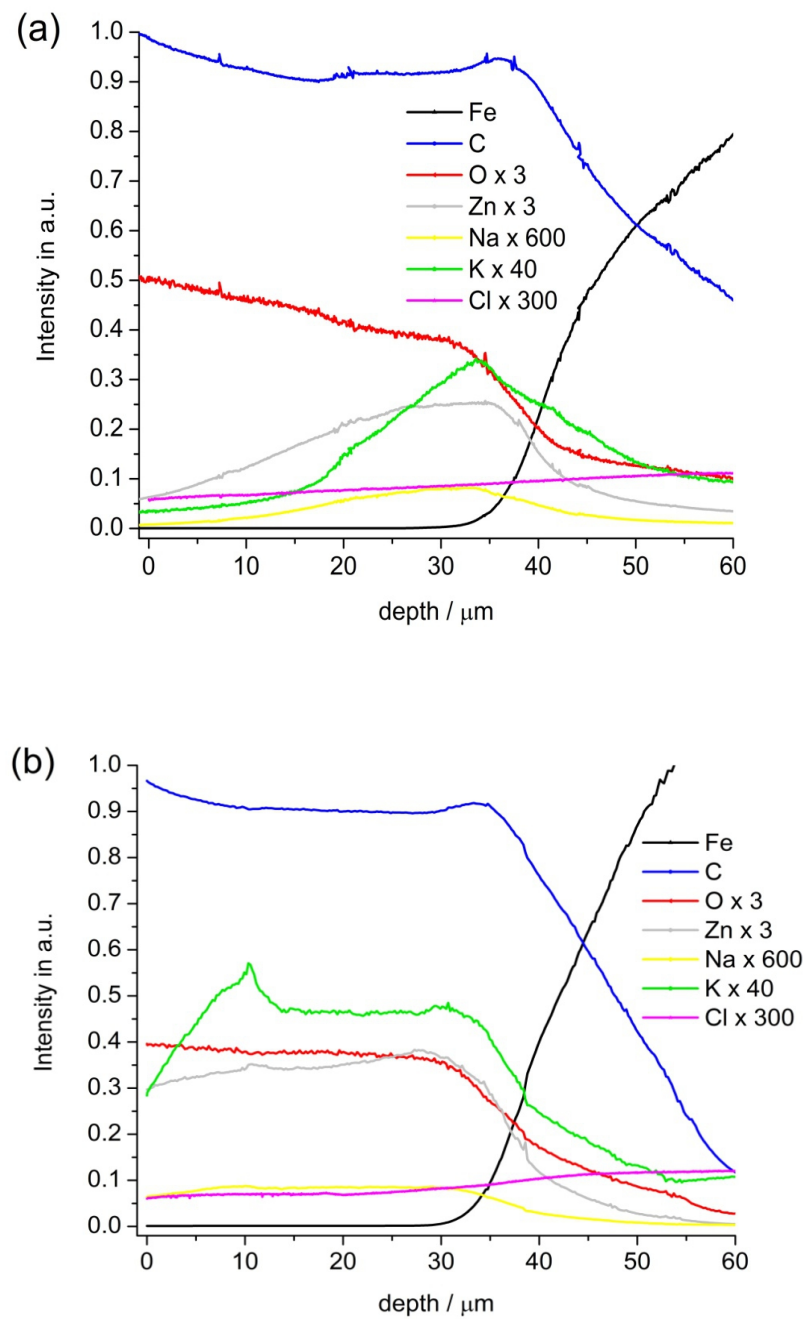
Figure 15. GD-OES depth profiled coating elements and corrosive analytes in the epoxy primer of *C4*: (a) before and (b) after the 254 days of immersion test.

Figure 16. GD-OES depth profiled coating elements and corrosive analytes in the epoxy primer of *C5*: (a) before and (b) after the 254 days of immersion test.

Figure 17. GD-OES depth profiled coating elements and corrosive analytes in the epoxy primer of *C6:* (a) before and (b) after the 254 days of immersion test.

However, the sensibly increased zinc bound oxygen measured in 20 μm thickness of the epoxy next to the steel surface (which was considerably lower than in the case of *ZA*) is

connected to the lower dispersity of the *p3* (compared to *p1* and *p2*) and the less comprehensive inhibition of zinc corrosion. Similar phenomenon was observed when ionic species were depth-profiled in coating *C4* as it is shown in Figures 15a and b. The only exception was noted as an undetectable change in the oxygen content, suggesting not only effective barrier nature but also limited galvanic function of the hybrid primer (partially as a consequence of the low activation of anodic zinc) loaded with completely incoherent flocs which are composed of strongly aggregated nanotube-supported filaments. Insignificant increments in the contents of oxygen and the ionic species in the *C5* were disclosed by the measured depth profile data presented in Figures 16a and b, remaining within the ranges of paint composition related fluctuations in the specific contents of the components. The impedance suggested decreasing efficacy of electrolytic barrier ability of the *C6* during the immersion test is corroborated by the detection of greater amount of potassium (by 3.3%) marked by the intensity difference near the solution interface shown in Figures 17a and b. This is accounted for the effect of the polyelectrolyte and the highly sulfonated nanotube contents of the *p6* PDIP sample with its strongly coherent microstructure resulting in the formation of well interconnected zinc pigments in the epoxy primer. These properties lead to the evolution of moderately intense galvanic characteristic which was indicated by the slightly cathodic OCPs and the decreasing amplitudes featured impedance spectra vs. time exposure.

X–Ray Photoelectron Spectroscopy

To characterize the paint-steel interface of the corrosion tested samples, XPS measurements were performed after removing paint coatings by sonication in appropriate solvents. The experiments gave information on the amount and the chemical state of interfacial iron oxides as well as those of paint residues.
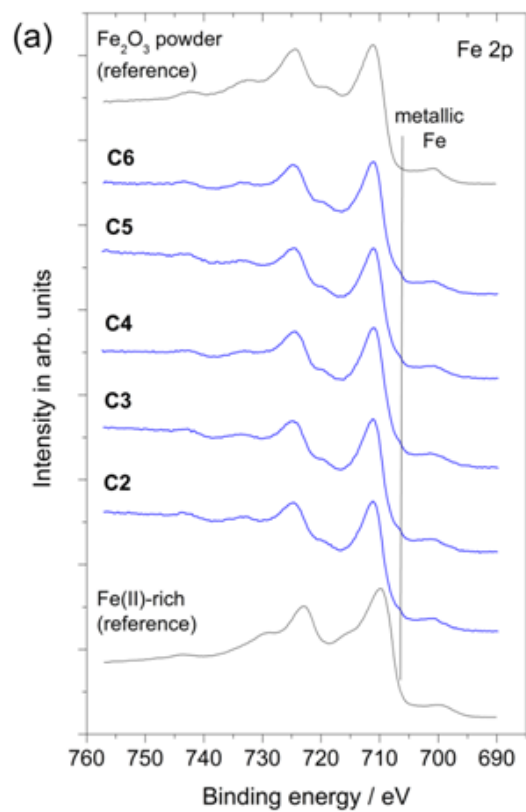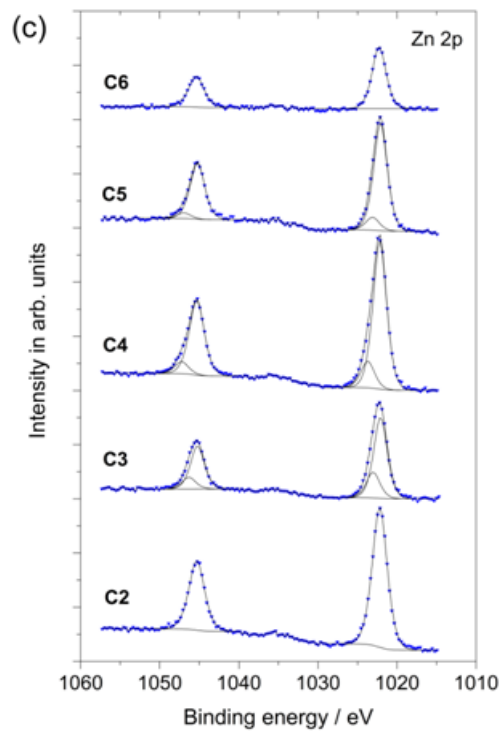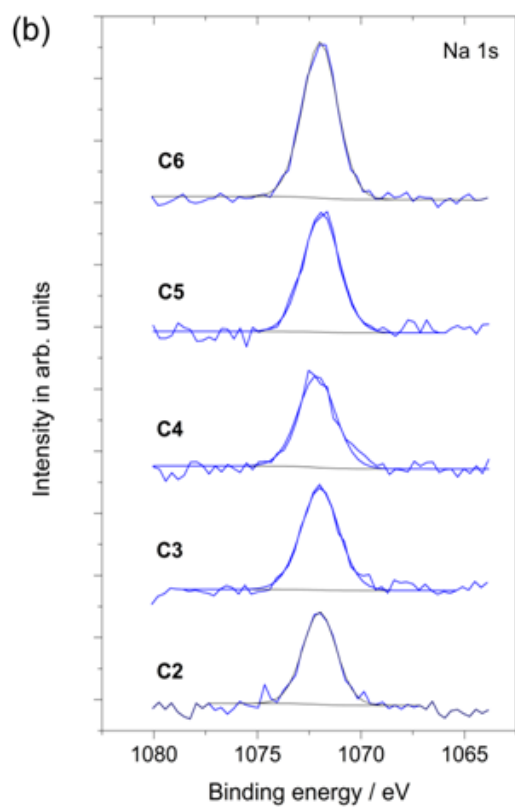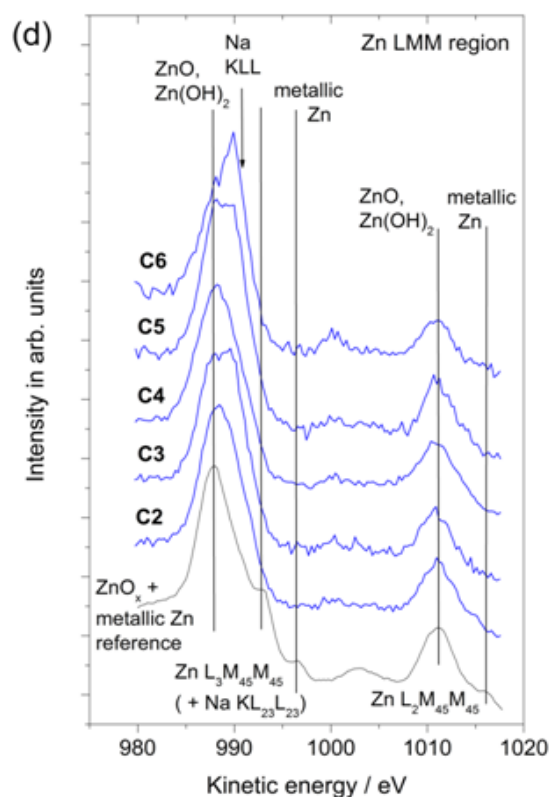
Figure 18. XPS spectra of particular regions measured in the paint-steel interface of the immersion tested paint coatings: (a) Fe 2p with the reference spectra of Fe_2O_3 powder (rich in Fe(III) states) and the Fe(II) rich evaporated thin film, (b) Na 1s, (c) Zn 2p and (d) the X-ray excited Auger Zn LMM spectra, where intensity of the peaks correlate with the element contents of the samples. A spectrum of a Zn oxide/hydroxide containing layer with some metallic Zn contribution is also shown as reference.

Figure 18a depicts the Fe 2p spectra of steel samples with the reference spectra of Fe(II)-rich iron oxide and Fe_2O_3 (containing Fe(III) states). Binding energy of the lowest energy structure, the Fe $2p_{3/2}$ peak is around 711.0 eV and the Fe 2p doublet is accompanied by satellites separated from the main peaks by 8.4 eV. These characteristics indicate the dominant form of iron in Fe(III) ionic state in the interface, although the weak shoulders shifted from the main peaks by 5-6 eV indicate the presence of Fe(II) ions as well. In addition, a weak feature around 707.0 eV indicates the presence of metallic iron, suggesting that thickness of the oxide layer is not enough to completely attenuate the signal arising from the underlying substrate. In fact, these features are characteristic for native iron oxides formed under ambient conditions [63]. Therefore, the oxide layer on the surface corresponds to the one formed before the application of paint coating, demonstrating the corrosion protection abilities of the paint formulations. Samples contained somewhat varying amounts of sodium as it is shown in Figure 18b (stronger peak corresponds to higher Na content), with *C6* being the most sodium-rich. Assignment of the sodium contribution is not particularly straightforward, as a significant part of Na compounds ranging from metallic Na to halides, phosphates or carbonates has a 1s binding energy around 1072.0 eV. Hence, the same value is

found in this work at the paint-steel surface. Nevertheless, because of the low chlorine level, NaCl is not a particularly probable interfacial compound in this case.

The intensity related contents of zinc presented in Figure 18c also varied from sample to sample. Under the coatings of *C2* and *C6*, rather symmetric Zn 2p$_{3/2}$ line was detected around 1022.1-1022.2 eV binding energy, while in the case of coatings *C3*, *C4* and *C5* more asymmetric peak shapes were obtained. In the latter cases fitting was accomplished by two components, with the minor contribution around or above 1023 eV. As far as the identification of the compounds contributing to the main zinc line is concerned in accordance with the literature data [64], metallic zinc as well as the range of zinc oxides and certain halides exhibit a 2p$_{3/2}$ binding energy around 1022 eV. Although the Zn LMM Auger line positions show pronounced variations in these materials [64], the exact overlap of the most intense Zn Auger peak and the Na KLL Auger line still complicates the analysis of the chemical state of Zn in the present samples. Nevertheless, data obtained on the Zn LMM Auger peak region are presented in Figure 18d. To assist peak assignment, a reference spectrum taken from zinc oxide/hydroxide surface is shown with some metallic zinc. It is obvious that the Zn L$_3$M$_{45}$M$_{45}$ structure measured at the paint-steel interface exhibits significant spectral intensity around the kinetic energy of 988 eV, which is characteristic for the zinc oxides. On the other hand, contributions from metallic zinc around 992-993 eV and 996-997 eV are missing, indicating that metallic Zn in the paint-steel interfaces is negligible. Still, there is a considerable spectral contribution around 990 eV, which is missing from the reference spectrum and whose intensity varies in accordance with the sodium contents of the samples. This peak can be thus assigned to the Na KL$_{23}$L$_{23}$ Auger line. Its kinetic energy around 990 eV is in agreement with the possible assignments given in the table. The minor Zn 2p$_{3/2}$ peak observed in the samples coated with *C3*, *C4* and *C5* can be assigned to a range of corrosion products such as ZnCl$_2$, zinc hydroxide or Zn(OH)$_x$(CO$_3$)$_y$ like compounds [65]. Potassium contents of the coatings are at or below the detection level of the experiment. The carbon content characterizes the amount of paint residues remaining on the surface after the solvent treatment, which varied a little from sample to sample. Nevertheless, the relative amounts of the oxidized carbon species showed only small variations, confirming the lack of severe oxidative degradation of the organic matrix in the interfacial region. Similarly, no strong variation in the O 1s line shape was observed, where the strongest component was always the metal-oxide related contribution. Qualitative evaluation of the XPS results based on the relative quantities of the main components provided important information on the corrosion resistive abilities of the paint coatings. These evaluation results are summarized in Table 5. As a comparison between the hydrophilic alumina contained zinc-rich *ZA* and the traditional type zinc-rich *Z*, the high relative proportion of zinc hydroxide compared to the contents of zinc oxide, iron oxide/hydroxide and carbon confirms an intense but low efficiency galvanic function of the *ZA* despite the EIS characterized low electrolytic permeability. This is signified by the comparison with the greater porosity featured but more efficiently functioning *Z*, exhibiting the accumulation of low quantity of zinc hydroxides along with the formation of similar relative amounts of iron oxide/hydroxide. Almost the same oxidative conversion, especially the carboxyl yield of epoxy suggests intense electron-transfer-reaction related galvanic function of the primers and the viable cathodic polarization driven ORRs, leading to severe degradation of the vehicle in the coating-steel interfacial region of the *ZA* and *Z*.

Table 5. The ratio of particular species based on the XPS quantification data acquired from the surface of immersion tested steel specimens

Forms of elements	E	Z	ZA	C1	C2	C3	C4	C5	C6
$ZnO_x(OH)_y$/ carbon content	-	0.23	0.46	0.05	0.08	0.04	0.10	0.04	0.04
$Zn(OH)_2$/ carbon content	-	0.01	0.05	0.01	<0.01	<0.01	0.01	<0.01	<0.01
$Zn(OH)_2$/ ZnO	-	0.05	0.12	0.21	~0.10	0.30	0.16	0.11	~0.10
$ZnO_x(OH)_y$/ $FeO_x(OH)_y$	-	0.43	0.79	0.22	0.18	0.13	0.21	0.15	0.07
$FeO_x(OH)_y$/ carbon content	-	0.52	0.58	0.25	0.46	0.30	0.46	0.28	0.57
COOH yield of epoxy (%)	2	11	12	8	7	6	3	6	5

Corresponding to the high porosity of zinc-rich Z, increased rate of sacrificial and self-corrosion of zinc is indicated by the amounts of carbon normalized zinc corrosion products, exceeding the ratio obtained for the all hybrid coatings. On the other hand, zinc corrosion products composed of not passivating hydroxides were detected around the same or even lower relative quantities on the steel surface coated with hybrid paints. Beyond the higher barrier nature of the $C1$–$C6$ hybrid coatings, the low amount of greater proportion of zinc hydroxides reflect on the active galvanic function of the primers with greater efficiency steel protection. The ratio of oxidized species of zinc and iron also showed a similar tendency. So, the relative quantities of the metallic iron compared to its oxidized forms became dominant for the Z and ZA coatings compared to other hybrid coatings except for the $C6$. In addition, the altered ratio of oxidized iron and the carbon contents is minor affected by the higher portion of paint residues on the surface of steel panels. This is in agreement with various degree of oxidative degradation – carboxyl yield of the epoxy binder and the related extent of de-adhesion, delamination of the coatings. Nonetheless, increased hydroxyl and carbonyl contents in $C4$ and $C6$ as well as the carboxyl conversion related oxidative degradation of epoxy in $C3$ and $C5$ are connected to the greater electrical bulk conductivity and galvanic function of the nanotube-loaded hybrid primers with the implied catalytic activity of the nanotubes for ORRs [77-79].

Salt-Spray Chamber Test

The wet and dry cycled salt mist test provided harsh enough environment to characterize all around corrosion resistive function of the paint coatings. Figures 19 and 20 depict coating samples from which the photos were taken right after drying and removing salt traces remained from the chamber test.
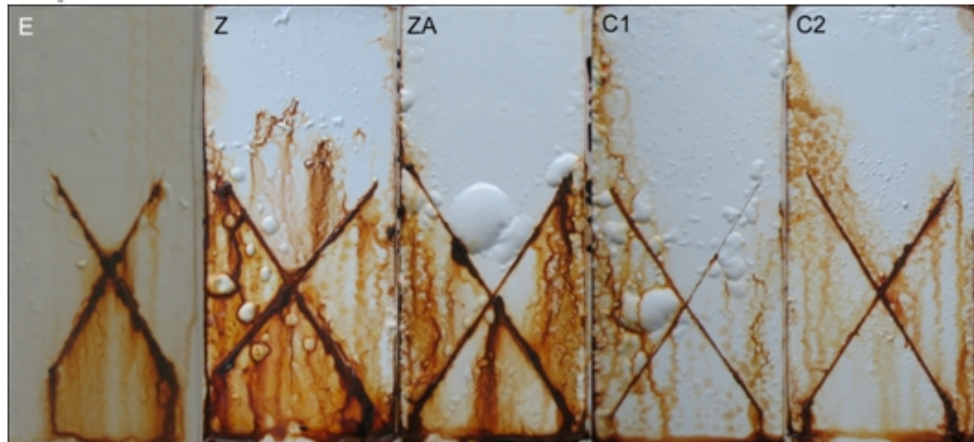
Figure 19. Photographs of cyclic salt-spray chamber tested paint coatings, after a 142 day period, except for the neat epoxy paint coating which was tested for 16 days.
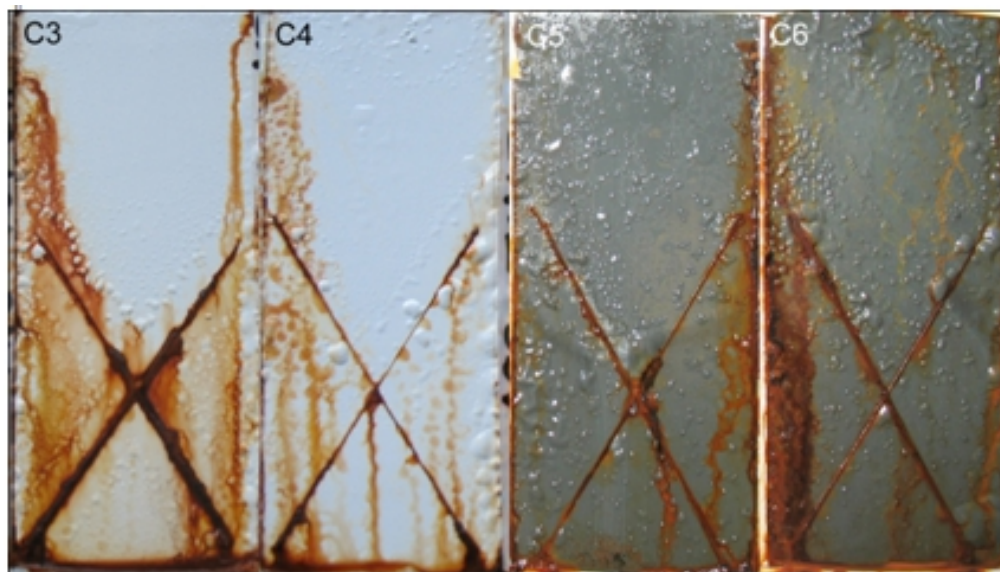

Figure 20. Photographs of cyclic salt-spray chamber tested paint coatings, after a 142 day period.

The neat epoxy (*E*) did not prevent rapid rust formation but exhibited fine condition at intact areas (Figure 19), according to the excellent passive protection ability of the pigment and particle-free paint coatings. Therefore, chamber test was terminated within 16 days. The alumina contained zinc-rich *ZA* indicated severe coating damages and stain formation around the X-cut which are attributed to the low electrical conductivity related poor galvanic function of the primer. However, the better condition of *ZA* compared to *Z* at the buried surface is connected to the highly dispersed nano-size alumina filler caused decreased porosity of the primer. Although efficient galvanic action of the *Z* was reflected by the slightly migrated delamination front around the cuts, the low resistivity against blistering and the intensity of

rusting support the idea of only moderate overall protection capability. In the case of hybrid coatings, the highly dispersed PPy-deposited alumina particles loaded *C1* indicated excellent rust inhibition but failed at coating delamination, which suggest intense but less efficient galvanic function of the primer. This is probably due to a somewhat decreased barrier profile of the coating. In contrast, *C2* exhibited very good state regarding all aspects of the usual measures. On the other hand, polyelectrolyte modified nanotube contained *C3* afforded moderate rust formation inhibition but excellent resistivity against delamination and blistering (Figure 20). Furthermore, the coatings of *C4* and *C5* provided superior steel protection reflected by the insignificant intensity steel rusting and strong resistance against delamination. However, the apparently low susceptibility to blistering was noted at the buried areas. In addition, the moderate protection ability of the *C6* is concluded based on the density and size of blistered spots and the intensity of steel rusting, besides the valuable active function against delamination (Table 6).

Table 6. Evaluation of salt-spray chamber test results corresponding to the EN ISO 4628-8:2005 standard, regarding degree of delamination and blistering of paint coatings and steel rusting

Coatings	Blistering size and density	Rusting	Delamination	
E	2	1	Ri 4	considerable
Z	3	2	Ri 3	slight
ZA	2	2	Ri 4	severe
C1	2	2	Ri 2	considerable
C2	2	2	Ri 2	very slight
C3	2	3	Ri 3	very slight
C4	3	2	Ri 3	slight
C5	3	3	Ri 3	slight
C6	3	2	Ri 2	slight

As for the repeatability of the experimental results, multiple coating samples were formulated for parallel corrosion test procedures. Immersion tests were repeated at the other surface area of the same coating and on another sample, indicating less than 10 relative percent differences in the state and lifetime of the coatings measured by the extent of scattering in the open-circuit potentials and the impedance data over the whole test periods. Quality assessment of the parallel samples was performed to comply with the ISO standard to gain overview about the repeatability of the all around protection characteristics of the paint coatings over certain time periods. The ongoing visual observation of the intensity, surface density and homogeneity of steel rusting and coating blistering were completed with checking the adhesion of the primers at the end of tests.

Minor differences in the corrosion resistive function are connected to the changes in the sub-micron dispersity of the inhibitor particles and their distribution in the epoxy around the zinc pigments, with some local fluctuation in the concentration of the highly anisotropic nanotube-embedded particles. These factors are mainly connected to the repeatability of the

paint formulation and film formation procedures (effect of grinding the particles, mixing and homogenizing paint dispersions).

Given the fact that electrical percolation is contributed by the higher nanotube contents than rheological percolation because effective restriction of the mobility of polymer chains becomes pronounced at lower nanotube concentration than the formation of extensive three-dimensional network for electron conduction [66-68] in epoxy around 0.5 wt.% [69,70]. Therefore, owing to the immersion and salt-spray chamber test results, it is highly obvious that nanotube-embedded anodic PDIPs have an influence on the galvanic efficiency, cathodic corrosion preventing function of the zinc-rich hybrid coatings at zinc content of 70 wt.% (25.7% by volume) compared to the conventional liquid ZRPs with 90 wt.% zinc contents (55.8% by volume). In hybrid paints, it is to be noted that concentration of the nanotubes was around or lower the theoretically and experimentally defined geometrical and rheological percolation – entanglement regime of the nanotubes. Due to the various degree of polymer-complex assembly caused aggregation and flocculation of the PDIPs, rheological percolation – effective interparticle interaction should not be experienced by rheology characterization. On the other hand, despite the low nanotube contents, effective contribution to the electrical contacts between the zinc pigments is expected to be affected by the application of higher proportion of auxiliary electrically conducting particles – nano-size alumina supported PPy whose concentration was around the percolation threshold in the inhibitor particles [59].

In addition, due to the XPS and RF-GD-OES indicated low intensity of zinc corrosion, high performance and durable corrosion resistance of the hybrid coatings are surmised to take advantage of additional function of the highly dispersed PDIPs beyond the lower rate of zinc corrosion, such as mediating the interfacial electron transfer reactions (allowing moderate cathodic polarization). Regarding the remarkably durable adhesion of the hybrid paints, PDIPs is accounted for scavenging oxidative radicals [71] and eliminating strong nucleophile agents [72-74] taking a vital role in preventing chemical corrosion processes. These functionalities are able to moderate degradation rate of the epoxy vehicle, accumulation and leaching of the corrosion products [75,76] as well as delaying cohesive and adhesive failure of the binder, thereby suppressing the processes which ultimately lead to cathodic delamination phenomena. All these aspects reflect on the positive influence of the PPy-modified carbon nanotubes on the corrosion preventive performance of the zinc-rich hybrid paint formulations over the traditional type ZRPs.

However, utilization of the nanotubes must meet some relevant requirements prior to successful adoption into real-life applications. These are the high exfoliation and even distribution of the particles to promote acceptable micro-scale homogeneity in the paint coatings, as well as suppressing catalytic activity towards oxygen reduction reactions [77-79]. In the present case, the latter is ensured by the uniform and compact PPy layer deposition helping to retain preferred physical and mask undesired chemical nature of the nanotubes. Thus, appropriate nano-particle compositions and paint formulations with the nanotubes are expected to initiate substantial improvement in the corrosion preventing function of the metal-rich primer coatings, thereby opening new vistas to multiple ranges of corrosion protection applications.

CONCLUSION

Although aqueous-ethanol-prepared PPy-deposited alumina particles contribute effectively to the corrosion preventive function of the zinc-rich epoxy primers, massive protection performance improvement is gained by the use of intimately structured anodic inhibitor particles composed of nano-size alumina and nanotube carriers supported PPy. This approach provides viable solution to the yet unresolved percolation and porosity related phenomena of the ZRPs, despite the filamentous-like aggregated microstructure caused lower micro-scale dispersity of the nanotube-incorporated particles.

As a result of well-balanced active–passive protection functionalities, optimal corrosion resistance is afforded by the hybrid paint coatings composited with polyelectrolyte-modified MWCNT (at 7.1×10^{-3} volume fraction) embedded particles containing polypyrrole in 3.56 wt. %. Furthermore, stable steel protection is provided against corrosion by the hybrid coatings with 5.0×10^{-3} and 7.0×10^{-4} volume fractions of the low sulfonated nanotubes at 5.79 and 7.54 wt.% polypyrrole contents in the inhibitor particles. Zinc-rich hybrid formulation with highly sulfonated MWCNT-embedded inhibitor particles provide intense galvanic function with somewhat lower efficiency barrier profile of the paint coatings at polypyrrole and nanotube volume fractions of 4.6×10^{-3} and 1.3×10^{-3}, respectively.

Firm protection ability of the hybrid coatings is connected to the enhanced redox properties and conductivity of the nanotube-supported and unexchangeable counter-ion doped PPy. Moreover, the electrical conductivity between the zinc pigments is effectively contributed since the efficacy of galvanic function of the zinc-rich hybrid primers is increased along with the inhibition of zinc corrosion and the improved barrier nature of the coatings. Moderate galvanic action of the hybrids takes longer time to develop but the evolved passive function of the coatings more durable than in the case of traditional liquid ZRPs. This is due to the enhanced barrier behaviour reinforced by the PPy-modified alumina/carbon nanotube inhibitor particles and the accumulation, long-term pore-filling corrosion products.

Owing to the limited exploitation of hybrid paints, zinc-rich primers containing polypyrrole modified nanotubes at low amounts are recognized as worthy candidates to be utilized in cost effective and environmentally friendly organic coating applications.

ACKNOWLEDGEMENT

REFERENCES

[1]   C. M. Abreu, M. Izquier, M. Keddam, X. R. Nóvoa and H. Takenouti, *Electrochim. Acta* 41, 240 (1996).
[2]   V. Zivica, *Bull. Mater. Sci.* 25, 371 (2002).
[3]   S. G. Real, A. C. Elias, J. R. Vilche, C. A. Gervasi and A. Di Sarli, *Electrochim. Acta* 38, 2029 (1993).

[4]   D. Pereira, J. D. Scantlebury, M. G. S. Ferreira and M. E. Almeida, *Corros. Sci.* 30, 1135 (1990).

[5]   C. M. Abreu, M. Izquierdo, P. Merino, X. R. Nóvoa and C. Pérez, *Corrosion* 55, 1173 (1999).

[6]   R. N. Jagtap, R. Nambiar, S. Z. Hassan and V. C. Malshe, *Prog. Org. Coat.* 58, 253 (2007).

[7]   J. R. Vilche, E. C. Bucharsky and C. A. Giúdice, *Corros. Sci.* 44, 1287 (2002).

[8]   S. Shreepathi, P. Bajaj and B. P. Mallik, *Electrochim. Acta* 55, 5129 (2010).

[9]   M. T. Rodríguez, J. J. Gracenea, J. J. Saura and J. J. Suay, *Prog. Org. Coat.* 50, 68 (2004).

[10] H. Shi, F. Liu and E.-H. Han, *Surf. Coat. Technol.* 205, 4532 (2011).

[11] R. N. Jagtap, P. P. Patil and S. Z. Hassan, *Prog. Org. Coat.* 63, 389 (2008).

[12] C. A. Gervasi, A. R. Di Sarli, E. Cavalcanti, O. Ferraz, E. C. Ducharsky, S. G. Real and J. R. Vilche, *Corros. Sci.* 36, 1963 (1994),

[13] H. Marchebois, M. Keddam, C. Savall, J. Bernard and S. Touzain, *Electrochim. Acta* 49, 1719 (2004).

[14] A. Meroufel and S. Touzain, *Prog. Org. Coat.* 59, 197 (2007).

[15] D. Wang and G. P. Bierwagen, *Prog. Org. Coat.* 64, 327 (2009).

[16] O. Øystein Knudsen, U. Steinsmo and M. Bjordal, *Prog. Org. Coat.* 54, 224 (2005).

[17] Y. Shao, C. Jia, G. Meng, T. Zhang and F. Wang, *Corros. Sci.* 51, 371 (2009).

[18] J. S. Hammond, J. W. Holubka, J. E. deVries and R. A. Dickie, *Corros. Sci.* 21, 239 (1981).

[19] M. A. Hernandez, F. Galliano and D. Landolt, *Corros. Sci.* 46, 2281 (2004).

[20] E. Armelin, M. Martí, F. Liesa, J. I. Iribarren and C. Alemán, *Prog. Org. Coat.* 69, 26 (2010).

[21] A. Meroufel, C. Deslouis and S. Touzain, *Electrochim. Acta* 53, 2331 (2008).

[22] Steven K. Geer and Todd R. Hawkins, *United States Patent* No**.** 7,595,009, Sept 29, 2009.

[23] Sze Cheng Yang and Wenguang Li Yang, *United States Patent* No**.** 6,803,446, Oct. 10, 2004.

[24] W. Wunderlich and M. Takahashi, Ceramic Transactions Vol. 133 Ed. M. Matsui, et al., Am. Ceram. Soc. (2002) pp 189–194.

[25] E. Akbarinezhad, M. Ebrahimi, F. Sharif, M. M. Attar and H. R. Faridi, Prog. Org. Coat. 70, 39 (2011).

[26] R. N. Rothon, *Adv. Polym. Sci.* 139, 67 (1999).

[27] J. I. Martins, T. C. Reis, M. Bazzaoui, E. A. Bazzaoui and L. Martins, *Corros. Sci.* 46, 2361 (2004).

[28] D. R. Paul and L. M. Robeson, *Polymer.* 49, 3187 (2008).

[29] G. Paliwoda-Porebska, M. Stratmann, M. Rohwerder and K. Potje-Kamloth, *Corros. Sci.* 47, 3216 (2005).

[30] J. Bonastre, P. Garcés, F. Huerta, C. Quijada, L. G. Andión and F. Cases, *Corros. Sci.* 48, 1122 (2006).

[31] P. Ocón, A. B. Cristobal, P. Herrasti and E. Fatas, *Corros. Sci.* 47, 649 (2005).

[32] B. N. Grgur, N. V. Krstajic, M. V. Vojnovic, C. Lacnjevac and Lj. Gajic-Krstajic, *Prog. Org. Coat.* 33, 1 (1998).

[33] M. Tiitu, A. Talo, O. Forsén and O. Ikkal, *Polymer.* 46, 6855 (2005).

[34] R. Partch, S. G. Gangolly, E. Matijevic, W. Cai and S. Arajs, *J. Coll. Interface Sci*. 144, 27 (1991).

[35] H. Chriswanto, H. Ge and G. G. Wallace, *Chromatographia* 37, 423 (1993).

[36] S. Maeda and S. P. Armes, *J. Mat. Chem*. 4, 935 (1994).

[37] A. Malinauskas, *Polymer* 42, 3957 (2001).

[38] M. Ionita and A. Pruna, *Prog. Org. Coat*. 72, 647 (2011).

[39] E. Akbarinezhad, F. Rezaei and J. Neshati, *Prog. Org. Coat*. 61, 45 (2008).

[40] J. F. Moulder W. F. Stickle, P. E. Sobol and K. D. Bomben, Handbook of X-Ray Photoelectron Spectroscopy, Perkin-Elmer Corp., Eden Prairie, Minnesota, USA (1992).

[41] C. D. Wagner, A. V. Naumkin, A. Kraut-Vass, J. W. Allison, C. J. Powell and J. R. Rumble Jr., NIST X-ray Photoelectron Spectroscopy Database, Version 3.4, National Institute of Standards and Technology, Gaithersburg, MD 2003, http://srdata.nist.gov/xps/

[42] N. Fairley, www.casaxps.com/

[43] M. Mohai, *Surf. Interface Anal.* 36, 828 (2004).

[44] M. Mohai, XPS MultiQuant: Multi-model X-ray photoelectron spectroscopy quantification program, Version 3.00.16 (2003), http://www.chemres.hu/aki/XMQpages/XMQhome.htm/

[45] S. Krishnakumar and P. Somasundaran, *Colloids Surf.* 117, 37 (1996).

[46] G. P. Funkhomer, M. P. Arévalo, D. T. Glatzhofer and E. A. O'Reart, *Langmuir.* 11, 1443 (1996).

[47] P. Somasundaran, *J. Phys. Chem.* 70, 90 (1966).

[48] D. Wu, W. Liang and Z. Ming, *J. Polym. Sci. B* 45, 2239 (2007).

[49] E. S. G. Shaqfeh and G. H. Fredrickson, *Phys. Fluids* A 2, 7 (1990).

[50] M. S. P. Shaffer, X. Fan and A. H. Windle, *Carbon* 36, 1603 (1998).

[51] M. Poorteman, M. Traianidis, G. Bister and F. Cambier, *J. Eur. Ceram. Soc.* 29, 669 (2009).

[52] M. Poorteman, P. Descamps, F. Cambier and A. Leriche, *J. Eur. Ceram. Soc.* 12, 103 (1993).

[53] C. M. Hansen, Hansen solubility parameters: a user's handbook CRC Press, 2007.

[54] G. Socrates, Infrared and Raman Characteristic Group Frequencies, 3rd edition, 2001, John Wiley and Sons, Ltd. Baffins Lane, Chichester, England, 182.

[55] B. Tian and G. Zerbi, *J. Chem. Phys*. 92, 3892 (1990).

[56] A. Gergely, É. Pfeifer, I. Bertóti, T. Török, E. Kálmán, Corr. Sci. 53, 3486 (2011).

[57] O. Patil, A. J. Heeger and F. Wudl, *Chem. Rev.* 88, 183 (1988).

[58] L. Liu, C. Zhao, Y. Zhao, N. Jia, Q. Zhou, M. Yan and Z. Jiang, *Europ. Polym. J.* 41, 2117 (2005).

[59] G. Cho, D. T. Glatzhofer, B. M. Fung, W.-L. Yuan and E. A. O'Rear, *Langmuir.* 16, 4424 (2000).

[60] P. A. Sorensen, K. Dam-Johansen, C. E. Einell and S. Kill, *Prog. Org. Coat.* 68, 283 (2010).

[61] T. Nguyen, J. B. Hubbard and J. M. Pommersheim, *J. Coat. Technol*. 68, 45 (1996).

[62] F. Deflorian and S. Rossi, *Electrochim. Acta* 51, 1736 (2006).

[63] G. Bhargava, I. Gouzman, C. M. Chun, T. A. Ramanarayanan and S. L. Bernasek, *Appl. Surf. Sci*. 253, 4322 (2007).

[64] S. Schürz, G. H. Luckeneder, M. Fleischanderl, P. Mack, H. Gsaller, A. C. Kneissl and G. Mori, *Corros. Sci.* 52, 3271 (2009).

[65] B. Zhang, H.-B. Zhou, E.-H. Han and W. Ke, *Electrochim. Acta* 54, 6598 (2009).

[66] Q. Zhang, S. Rastogi, D. Chen, D. Lippits and P. J. Lemstra, *Carbon* 44, 778 (2006).

[67] J. Sumfleth, S. T. Buschhorn and K. Schulte, *J. Mater. Sci*. 46, 659 (2011).

[68] J. Zhu, S. Wei, A. Yadav and Z. Guo, *Polymer.* 51, 2643 (2010).

[69] Y. S. Song and J. R. Youn, *Carbon* 43, 1378 (2005).

[70] Y. J. Kim, T. S. Shin, H. D. Choi, J. H. Kwon, Y. C. Chung and H. G. Yoon, *Carbon* 43, 23 (2005).

[71] M. N. Ismail, M. S. Ibrahim and M. A. A. El-Ghaffar, *Polym. Degrad. Stab*. 62, 337 (1998).

[72] T. Osaka, T. Fukuda, K. Ouchi and T. Momma, *Thin Solid Films* 215, 200 (1992).

[73] O. Inganäs, R. Erlandsson, C. Nylander and I. Lundström, *J. Phys. Chem. Solids* 45, 427 (1984).

[74] F. Beck, P. Braun and F. Schloten, *J. Electroanal. Chem.* 267, 141 (1989).

[75] G. Grundmeier, W. Schmidt and M. Stratmann, *Electrochim. Acta* 45, 2515 (2000).

[76] G. Williams, R. J. Holness, D. A. Worsley and H. N. McMurray, *Electrochem. Commun.* 6, 549 (2004).

[77] X. Y. Zhu, S. M. Lee, Y. H. Lee and T. Frauenheim, *Phys. Rev. Lett*. 85, 2757 (2000).

[78] G. Jürmann and K. Tammeveski, *J. Electroanal. Chem*. 597, 119 (2006).

[79] I. Kruusenberg, N. Alexeyeva and K. Tammeveski, *Carbon* 47, 651 (2009).